J. Fluid Mech. (1997), *vol.* 345, *pp.* 165–201. Printed in the United Kingdom

© 1997 Cambridge University Press

Dynamics of monopolar vortices in a strain flow

By R. R. TRIELING†, M. BECKERS AND G. J. F. VAN HEIJST

Fluid Dynamics Laboratory, Department of Technical Physics, Eindhoven University of Technology, PO Box 513, 5600 MB Eindhoven, The Netherlands

(Received 31 October 1996 and in revised form 15 April 1997)

The strain-induced evolution of shielded monopolar vortices has been investigated in a stratified fluid. A steady strain flow was generated by an arrangement of four rotating horizontal discs, whereas the monopolar vortex was created by a small spinning sphere. Quantitative information about the flow field was obtained by tracking passive tracer particles. The vortex was observed to deform into a tripolar-like structure, followed by the shedding of the accompanying satellites. During this stage, the remaining vortex core evolved quasi-steadily, which was evident from the functional relationship between the vorticity and the stream function. Furthermore, it was shown that the removal of the surrounding ring of oppositely signed vorticity induces an accelerated horizontal growth of the vortex core. Owing to the diffusive decay of vorticity, the vortex was finally torn apart along the horizontal strain axis. The dynamics of the vortex core appeared to be very similar to that of an elliptic patch of uniform vorticity. The instantaneous vorticity contours at high vorticity levels were close to ellipses with nearly the same aspect ratios and orientations. Moreover, the observed vortex evolution was in qualitative agreement with the calculated motion of an elliptic patch of uniform vorticity. As a second approach, the full two-dimensional vorticity equation was solved numerically by a finite-difference method in order to account for both the non-uniform spatial vorticity distribution of the laboratory vortex and the diffusion of vorticity in the horizontal directions. The numerically obtained vortex evolution was in good agreement with that observed in the laboratory.

1. Introduction

Two-dimensional vortices abound in large-scale geophysical flow systems, such as the planetary atmospheres and the world's oceans. In these situations, two-dimensionality is mainly caused by planetary background rotation and density stratification, as well as by constraints imposed by the geometry of the flow domain (i.e. the ocean and atmosphere being shallow layers covering the Earth). Generally, two-dimensional vortices may undergo serious deformations due to a non-uniform ambient flow induced by neighbouring vortices or global currents. As a first approximation, such a non-uniform background flow may be considered as a (uniform) shear flow. Typical examples of vortices in strongly shearing east-west winds are the Great Red Spot of the planet Jupiter, which has been observed for more than 300 years, and the Great Dark Spot of Neptune.

† Present address: Royal Netherlands Meteorological Institute, PO Box 201, 3730 AE De Bilt, The Netherlands.

https://doi.org/10.1017/S0022112097006356 Published online by Cambridge University Press

An interesting analytical solution for an unsteady elliptic vortex in a uniform shear flow was found by Chaplygin (1899) and independently by Kida (1981) (see Meleshko & van Heijst 1994 for an overview of Chaplygin's earlier work). Depending on the relative magnitudes of the uniform vorticity in the vortex and that of the shear flow, the vortex may exhibit various types of motion, such as rotation and shape oscillations. This model was recently applied to analyse the observed motion of Neptune's Great Dark Spot (see Polvani *et al.* 1990).

In the last few years, a number of interesting results concerning vortices in strain and shear flows have been obtained from numerical simulations. For example, numerical studies by Dritschel (1989) and Legras & Dritschel (1993, 1994) have shown that for a vortex with a non-uniform vorticity distribution embedded in a shear flow, low-amplitude vorticity is being removed from the edge of the vortex, a phenomenon called 'vortex-stripping'.

However, only a few experimental studies have been performed related to this subject. As far as we are aware, laboratory observations of a vortex in a strain field have only been reported by Brickman & Ruddick (1990), who considered the effect of a time-dependent strain flow on a lens in a rotating fluid, and by Paireau, Tabeling & Legras (1997), who examined the deformation of monopolar vortices in an approximately uniform shear flow.

Given the fact that monopolar vortices are the most frequently observed vortex structures in nature and that their deformations are induced only by the straining part of the shear flow, the present paper will deal with the dynamics of monopolar vortices in a strain flow. The investigation is based on laboratory experiments which have been performed in a stratified fluid. The strain flow was established by four rotating discs, whereas the monopolar vortex was generated by a small spinning sphere. Quantitative information about the flow field was obtained by tracking passive tracer particles.

The laboratory observations will be compared with Kida's analytical model, which will be extended to account for the observed decay of vorticity. As a second approach, the full two-dimensional vorticity equation will be solved numerically by a finite-difference method, and the corresponding results will be compared with the laboratory observations.

This paper is organized as follows. After the description of the experimental set-up in § 2, the measured characteristics of the strain flow and the monopolar vortex will be presented in § 3 and § 4, respectively. In § 5, the observed evolution of monopolar vortices in strain flows is discussed, and in § 6 a comparison is made with the results obtained from the theoretical models. Finally, in § 7, the experimental and theoretical findings of this study will be summarized and the main conclusions will be given.

2. Experimental arrangement

The experiments were carried out in a square tank of inner dimensions $100 \times 100 \times 30$ cm (length $\times$ width $\times$ depth), which was filled with a two-layer salt stratification. Typically after a few days, an approximately linear density stratification was formed near the mid-plane of the tank within a horizontal layer of about 10 cm thickness. The fluid depth was about 26 cm and the buoyancy frequency N at mid-depth was varied between 1.6 and 3.4 rad s^{-1}.

The strain flow was generated by four rotating horizontal discs (diameter 10 cm, thickness 0.5 cm), which were positioned at the corners of a square in the mid-plane of the tank (see figure 1). The diagonal distance D between the centres of the discs was either 40 or 50 cm, and the discs were rotated continuously at a constant angular

https://doi.org/10.1017/S0022112097006356 Published online by Cambridge University Press

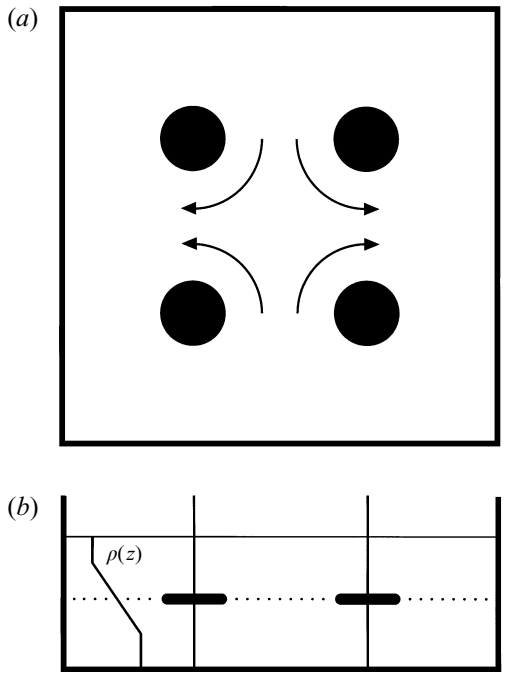


FIGURE 1. Schematic drawing of the top view (*a*) and the side view (*b*) of the laboratory set-up. The experiments were performed in a 100 × 100 cm Perspex tank with a working depth of 30 cm. A linear density stratification is present near the mid-level of the tank. The strain flow is generated by four rotating horizontal discs, which rotate continuously at a constant angular speed Ω_d. The diagonal distance D between the discs was either 40 or 50 cm. In order to measure the horizontal flow characteristics, passive tracer particles have been added to a horizontal layer of the fluid, which also contains the four rotating discs.

speed Ω_d in the directions indicated in figure 1 (*a*). The system was driven by a single motor to ensure that each disc had the same rotation speed.

Typically 1 h after the start of the strain flow forcing, a monopolar vortex was generated in the centre of the mid-plane by a small sphere (with a diameter of 2.5 cm) spinning about its vertical axis. For the experiments presented in this paper, the rotation speed of the sphere, Ω_s, was varied between 150 and 279 r.p.m., and the corresponding forcing period ranged from 5 to 15 s. After the spinning was stopped (at $t = 0$), the sphere was carefully removed from the tank.

In order to determine the horizontal velocity field, small polystyrene particles of density 1.04 g cm^{-3} were added to the fluid at the mid-level of the tank. The passive tracers were monitored continuously by a video camera which was mounted above the tank. Afterwards, the particles in successive digitized video images were linked together, using the image analysis system DigImage developed by Dalziel (1992). In this way, the local velocity vectors could be determined at successive times. The experimental error in the velocity values thus obtained was typically 3% of the maximum velocity. Next, the measured velocity vectors were calculated at the mesh points of a rectangular grid of 30 × 30 points by a spline-interpolation method (see Paihua Montes 1978 and Nguyen Duc & Sommeria 1988). The vorticity (ω), horizontal divergence ($\partial u/\partial x + \partial v/\partial y$), and local strain rates ($\partial u/\partial x$ and $\partial v/\partial y$) could be calculated at each grid point by differentiation of the splines, and were estimated to be accurate to within 6% of their corresponding maximum values. Likewise, the

https://doi.org/10.1017/S0022112097006356 Published online by Cambridge University Press

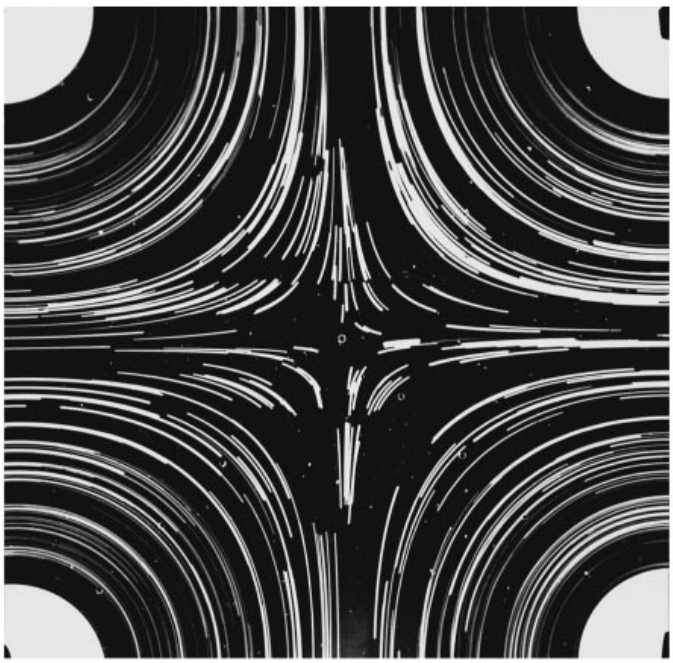


FIGURE 2. Photograph showing the trajectories of the tracer particles in the mid-plane of the tank, 4 h after the start of the forcing. The flow was generated by four rotating horizontal discs, and the strain rate e near the centre of the tank was 0.80×10^{-2} s^{-1}. The photograph was taken with an exposure time of 120 s. Experimental parameters: $\Omega_d = 3.0$ r.p.m., $D = 50$ cm and $N = 2.8$ rad s^{-1}.

stream function ψ, defined by $\boldsymbol{u}_h = -\boldsymbol{k} \times \nabla\psi$ (with $\boldsymbol{u}_h$ the horizontal velocity and $\boldsymbol{k}$ the unit vector in the upward direction), was obtained from the interpolated velocity field by numerical integration.

3. Strain flow characteristics

The strain flow pattern is clearly visible from the photograph in figure 2, which shows the trajectories of the passive tracers at the mid-plane of the tank. The path lines appear to be smooth and do not cross each other, which indicates that the flow is laminar and that the particles are moving on a two-dimensional surface. In fact, the flow is approximately planar since the particles are neutrally buoyant. Furthermore, the flow is characterized by a stagnation point and two symmetry axes, and from the lengths of the particle paths it can be seen that the absolute velocity of the fluid increases at larger radii from the stagnation point.

For a pure strain flow, with the Cartesian coordinates (x, y) taken along the symmetry axes of the flow, the corresponding velocity components would be

$$u(x, y) = ex, \quad v(x, y) = -ey, \tag{3.1}$$

respectively, where the origin coincides with the stagnation point and e is the strain rate.

The measured velocity vectors, obtained from the digitized particle paths, are plotted in figure 3 for one moment of time. To examine whether (3.1) holds for this observed velocity field, for each velocity vector depicted in figure 3 the velocity components u and v are plotted versus the spatial coordinates x and y, respectively

https://doi.org/10.1017/S0022112097006356 Published online by Cambridge University Press

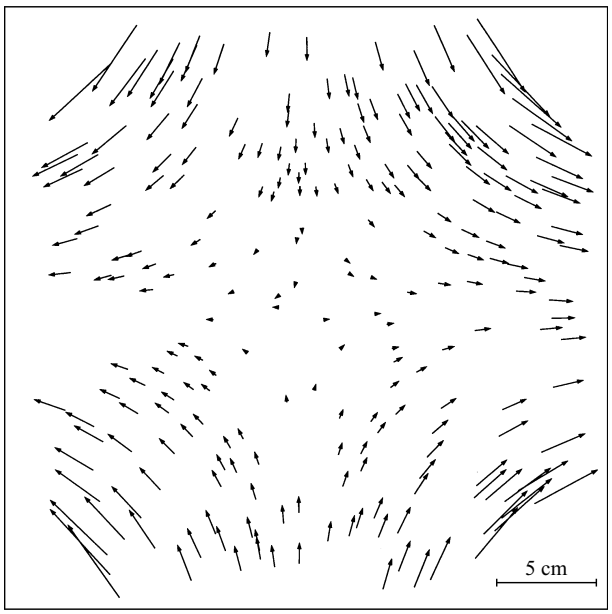


FIGURE 3. Measured velocity vectors as obtained from the digitized particle paths, 120 min after the start of the strain flow forcing. The largest vector corresponds to a velocity of 0.142 cm s^{-1}, and the strain rate e near the stagnation point of the flow was equal to $(0.283 \pm 0.003) \times 10^{-2}$ s^{-1}. Experimental parameters: $\Omega_d = 1.9$ r.p.m., $D = 50$ cm and $N = 2.8$ rad s^{-1}.

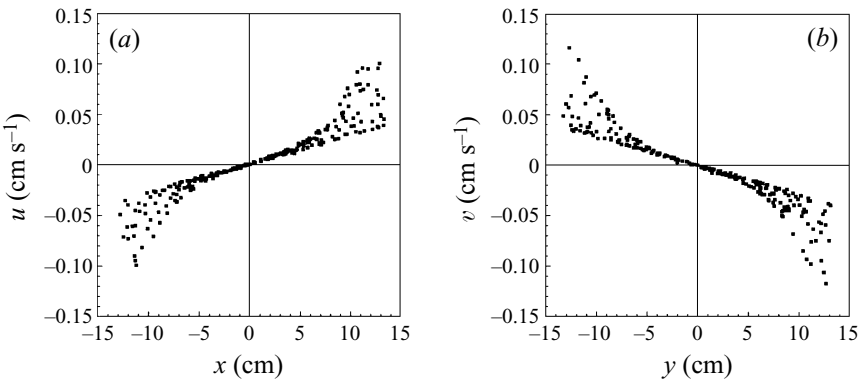


FIGURE 4. (*a*) Velocity component u versus x, and (*b*) velocity component v versus y, as obtained from each measured velocity vector depicted in figure 3. Experimental parameters as in figure 3.

(see figure 4), and substantial scatter is found close to the rotating discs ($D = 50$ cm). However, in the centre of the flow field a linear relationship is found, and the scatter can be eliminated by only considering the velocity vectors within a specific circular region around the stagnation point. Figure 5 shows the velocity data obtained within a bounding circle of radius $R_b = 8$ cm, and a good linear relationship is observed for each graph.

In order to determine the strain rate within this confined region, each reduced data set was least-square fitted with the relations $u = e_1(x + x_0)$ and $v = -e_2(y + y_0)$, respectively. The parameters x_0 and y_0 were introduced to account for a possible shift of the stagnation point, but in view of the experimental errors their values were

https://doi.org/10.1017/S0022112097006356 Published online by Cambridge University Press

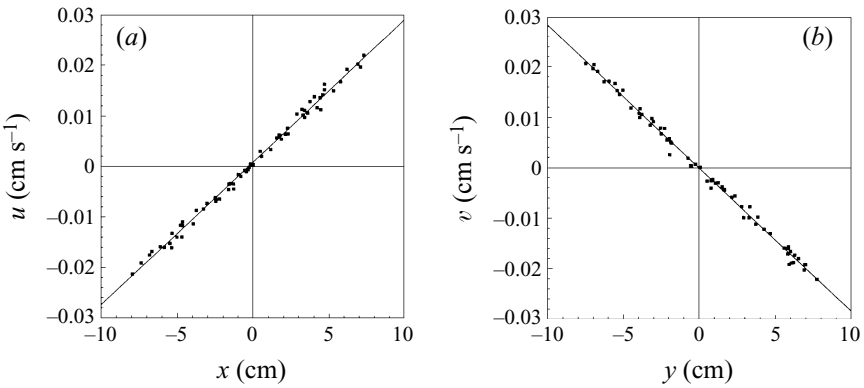


FIGURE 5. (*a*) Velocity component u versus x, and (*b*) velocity component v versus y. The experimental data (squares) correspond to the velocity vectors in figure 3 within the region enclosed by a circle of radius 8 cm. The straight lines correspond to linear least-square fits. Experimental parameters as in figure 3.

negligibly small. For the data shown in figure 5, the slopes e_1 and e_2 are both equal to $(0.283 \pm 0.003) \times 10^{-2}$ s^{-1}. Obviously, a pure strain flow is present within this limited region.

This assertion is supported by figure 6 (*a*), which provides the vorticity contours of the measured flow field. The vorticity contour plot reveals that the flow is irrotational in the central region, i.e. the magnitude of vorticity is of the same order as the experimental errors. The non-zero vorticity values near to the rotating discs explain why the corresponding velocity field deviates from a pure strain flow.

In figure 6 (*b*) a contour plot of the stream function is shown, and a good agreement is observed with the path lines in figure 2. Apparently, the strain flow generated is (quasi) steady, which will be confirmed by the measured time evolution of the strain rate (see later on).

Calculation of the horizontal divergence $\partial u/\partial x + \partial v/\partial y$ revealed that, except for a small region around the discs, this quantity was approximately zero, which implies that within the region of interest vertical motions can be neglected, i.e. the flow is mainly horizontal. The non-zero divergence values near the discs are caused by three-dimensional effects. That is, at the disc's upper and lower surfaces a boundary layer is present in which fluid is accelerated. As a result, close to the edge of the disc, fluid is swept radially outward and a turbulent region is formed, which causes vertical motions.

In figure 6 (*c*,*d*) contours of $\partial u/\partial x$ and $\partial v/\partial y$ are shown which represent the local strain rates in the x- and y-directions, respectively. Obviously, the local strain rate values are constant near the centre of the flow, implying a uniform strain flow, but they increase when approaching the rotating discs. This observation is supported by figure 4, which shows that the slopes of the relations $u(x)$ and $v(y)$ are constant within the central region of the flow, but become steeper at larger radii.

In order to investigate the stationarity of the generated strain flow, the temporal evolution of the strain rate e is plotted in figure 7 for four different experiments. The strain rates were calculated by linear regression of plots such as figure 5 and by taking the average of the corresponding values e_1 and e_2, i.e. $e = (e_1 + e_2)/2$. The bounding radius R_b was varied, depending on the diagonal distance D (see table 1). In all cases it was observed that the strain rate increased in time and tended towards

https://doi.org/10.1017/S0022112097006356 Published online by Cambridge University Press

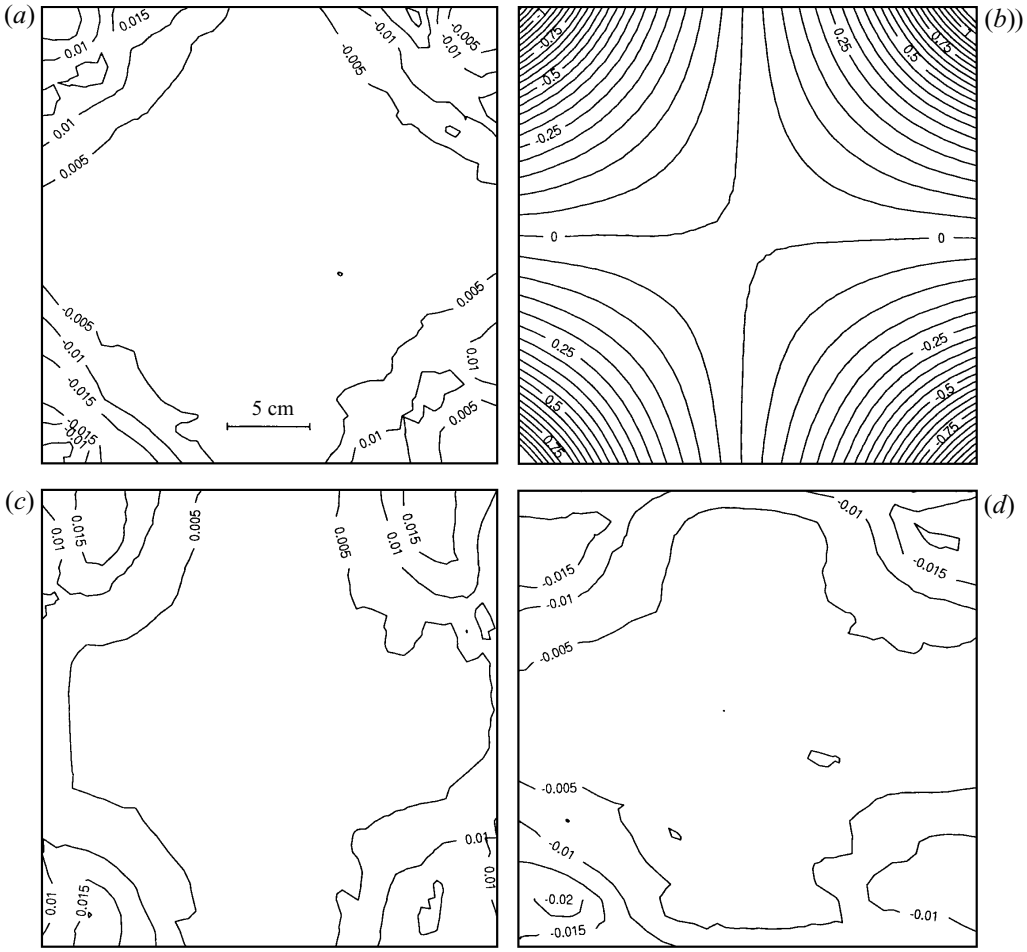


FIGURE 6. Contour plots of (*a*) vorticity ω and (*b*) stream function ψ, along with the local strain rates (*c*) $\partial u/\partial x$ and (*d*) $\partial v/\partial y$. The vorticity and local strain rate values are given in units of s^{-1}, whereas the stream function values are displayed in units of $cm^2\,s^{-1}$. Experimental parameters as in figure 3.

a constant value. Therefore, each data set was least-square fitted with the relation

$$e(t; e_\infty, \tau, t_b) = e_\infty \left[1 - \exp\left(\frac{t_b - t}{\tau}\right)\right], \tag{3.2}$$

where the free parameters are written explicitly, and a good agreement was obtained in each case. Here, e_∞ and τ represent the stationary strength and the characteristic generation time, respectively, whereas t_b is the time elapsed before the strain flow developed inside the bounding circle with radius R_b. The experimental parameters as well as the values obtained for e_∞, τ and t_b are listed in table 1.

The effect of D on the time evolution of the strain rate can be seen by comparing experiment 3 ($D = 40$ cm, squares) with experiment 4 ($D = 50$ cm, circles). In both cases $\Omega_d = 6.4$ r.p.m.. It is observed that when the discs are positioned further apart, t_b increases, whereas e_∞ remains nearly constant. Also the dependence on the rotation speed of the discs can be examined by comparing experiment 2 ($\Omega_d = 3.0$ r.p.m., triangles) with experiment 4 ($\Omega_d = 6.4$ r.p.m., circles). In both cases $D = 50$ cm. It

https://doi.org/10.1017/S0022112097006356 Published online by Cambridge University Press

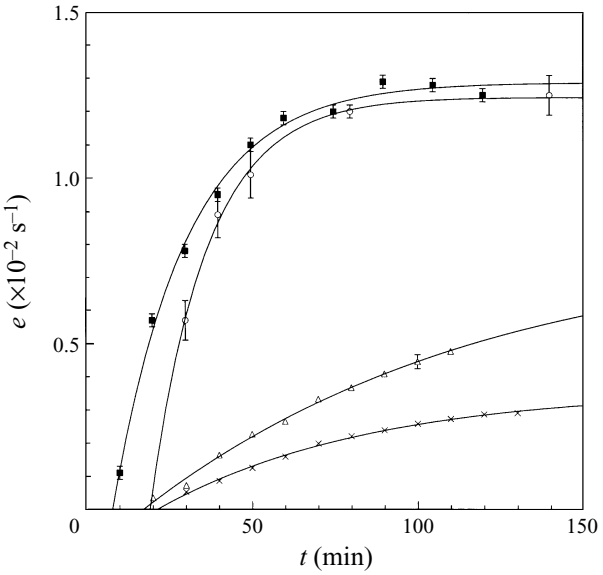


FIGURE 7. Temporal evolution of the strain rate e for four different experiments: experiment 1 (crosses), experiment 2 (triangles), experiment 3 (squares) and experiment 4 (circles). Experimental parameters: see table 1.

Exp. no.	Ω_d (r.p.m.)	D (cm)	N (rad s^{-1})	R_b (cm)	e_∞ (10^{-2} s^{-1})	τ (min)	t_b (min)
1	1.9	50	2.8	8	0.36 ± 0.02	64 ± 6	21.4 ± 1.3
2	3.0	50	2.8	8	0.81 ± 0.11	104 ± 21	17.2 ± 1.4
3	6.4	40	2.1	5	1.29 ± 0.02	23 ± 2	7.8 ± 0.6
4	6.4	50	2.8	8	1.24 ± 0.05	18 ± 5	19.0 ± 3.6

TABLE 1. Experimental parameters (columns 2–5) and results obtained from least-square fits with (3.2) for four laboratory experiments in which the time evolution of the strain rate was investigated. The symbols are defined in the text.

is seen that an increasing rotation speed causes e_∞ to increase, whereas t_b remains virtually constant. The present results are, however, not decisive about the dependence of τ on the experimental parameters.

One might wonder by which physical process the strain flow is accomplished. If the strain flow were established purely by viscous diffusion, the time scale would be $T_d \sim L^2/\nu$, with L a characteristic length scale and ν the kinematic viscosity. Taking the typical laboratory values $L = D/2 \sim 25$ cm and $\nu \sim 10^{-2}$ cm^2 s^{-1}, it follows that $T_d \sim 16$ h, which is much larger than the characteristic generation time τ. Therefore, viscous diffusion cannot account for the relatively fast genesis of the strain flow. Apparently, the strain flow is achieved by a mechanism far more effective than viscous diffusion, such as a secondary circulation induced by the rotating discs. However, further details on the development of the strain flow requires knowledge about the three-dimensional evolution of the flow field, information that is not available at present.

Nevertheless, from the laboratory observations presented above it can be concluded that a pure strain flow can be established near the centre of the tank when the flow

https://doi.org/10.1017/S0022112097006356 Published online by Cambridge University Press

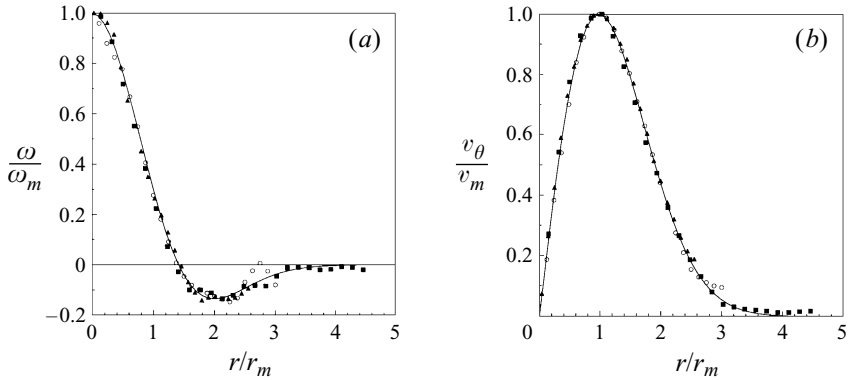


FIGURE 8. Measured cross-sectional distributions of (*a*) vorticity ω and (*b*) azimuthal velocity v_θ for a vortex generated by the spinning sphere, at three different times: $t = 120$ s (squares), 480 s (circles) and 720 s (triangles). Both ω and v_θ have been scaled with their extremal values ω_m and v_m, respectively, whereas the radial coordinate r has been scaled with the position of the peak velocity r_m. The measured data are compared with the corresponding vorticity and velocity profiles of the Gaussian vortex (solid lines). Experimental parameters: $\Omega_d = 150$ r.p.m., $\delta t = 15$ s and $N = 2.9$ rad s^{-1}.

is generated by four rotating horizontal discs in a stratified fluid. This was evident quantitatively from the linear relationships between the velocity components and the spatial coordinates, the zero vorticity, the zero horizontal divergence, the stream function, the constant local strain rates, and qualitatively from the particle path photographs.

Furthermore, it was observed that the strain rate evolves towards a constant value e_∞ within the characteristic time τ. Therefore, the monopolar vortex was generated at least a period τ after the start of the strain flow forcing to ensure an approximately constant strain flow during the temporal evolution of the vortex.

4. Monopolar vortices in still ambient fluid

The evolution of vortices generated by a spinning sphere has been studied in detail by Flór & van Heijst (1996) and Trieling & van Heijst (1997). Here, only a short outline will be given. For more details, the reader is referred to the above-mentioned papers.

In figure 8 typical measured distributions of vorticity ω and azimuthal velocity v_θ are shown (indicated by symbols) for a monopolar vortex generated by a spinning sphere. The experimental data between the grid points were obtained by bilinear interpolation. The vorticity and velocity profiles correspond to three different times, and for each time they have been scaled with their extremal values ω_m and v_m, respectively. Furthermore, the radial position of the peak velocity r_m, which is a measure of the vortex radius, has been used to normalize the radial coordinate r, according to $r^* = r/r_m$. It is apparent that the observed distributions at different times all collapse into a single curve, which implies that the profiles are self-similar in time.

The measured profiles can be closely approximated by the self-similar distributions of the so-called Gaussian vortex (solid lines in figure 8), which are given by

$$\omega^* = \left[1 - \tfrac{1}{2}(r^*)^2\right] \exp\left\{-\tfrac{1}{2}(r^*)^2\right\} \tag{4.1}$$

https://doi.org/10.1017/S0022112097006356 Published online by Cambridge University Press

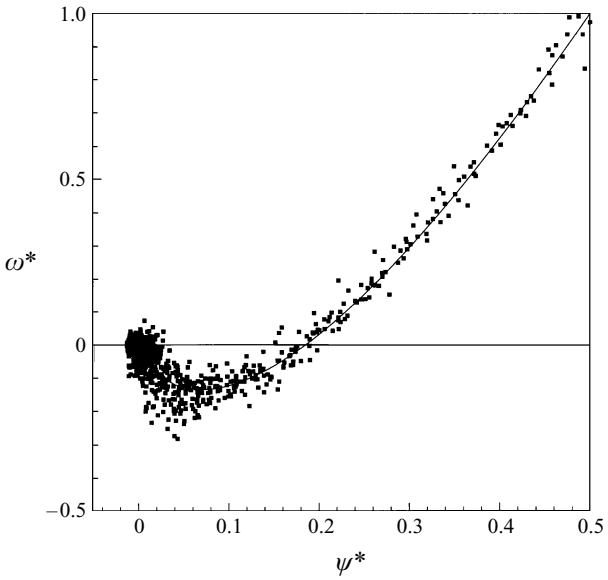


FIGURE 9. Characteristic (ω^*, ψ^*)-plot for a vortex generated by a spinning sphere. The vorticity ω and stream function ψ have been scaled according to relations (4.1) and (4.3), respectively. The experimental data at $t = 420$ s (denoted by squares) are compared with the (ω^*, ψ^*)-relationship (4.4) of the Gaussian vortex. Experimental parameters as in figure 8.

and

$$v^* = \tfrac{1}{2} r^* \exp\left\{-\tfrac{1}{2}(r^*)^2\right\}, \tag{4.2}$$

respectively, where $\omega^* = \omega/\omega_m$ is the scaled vorticity and v^* is the corresponding normalized azimuthal velocity. Here, the name 'Gaussian' refers to the Gaussian shape of the stream function distribution given by (4.3).

As can be seen from figure 8 (*a*), the Gaussian vortex is typified by a core of single-signed vorticity and a ring of oppositely signed vorticity. Moreover, the Gaussian vortex is 'shielded' or 'isolated', i.e. the vortex has no net vorticity. This was checked by taking the summation of the measured vorticity values $\omega_{i,j}$ over all the grid points (i, j) according to $\sum_{i,j} \omega_{i,j} \Delta x \Delta y$, where $\Delta x \Delta y$ represents the surface of one mesh. The dimensions of the grid were chosen such that the monopolar vortex (i.e. at least twice the core radius) was located well inside the computational domain. The total circulation of the vortex appeared to be zero within the experimental errors.

The corresponding non-dimensional stream function can be derived from (4.2), and is given by

$$\psi^* = \tfrac{1}{2} \exp\left\{-\tfrac{1}{2}(r^*)^2\right\}, \tag{4.3}$$

with ψ^* being chosen such that $\omega^* = -\nabla^2 \psi^*$.

Furthermore, the functional relationship F between ω^* and ψ^* can be obtained from (4.1) and (4.3), yielding

$$\omega^* = F(\psi^*) = 2\psi^* \left[1 + \ln 2\psi^*\right], \tag{4.4}$$

and is depicted in figure 9 by the solid line. This theoretical relationship was compared with laboratory observations by plotting in the same figure the measured values (ω^*, ψ^*) that correspond to the 900 grid points. Clearly, a good agreement exists.

https://doi.org/10.1017/S0022112097006356 Published online by Cambridge University Press

Exp. no.	Ω_d (r.p.m.)	D (cm)	N (rad s^{-1})	t_f (min)	R_b (cm)	$e(t_f)$ (10^{-2} s^{-1})	Ω_s (r.p.m.)	δt (s)
5	0.0	—	2.9	—	—	0	150	15
6	1.9	50	2.8	150	8	0.303 ± 0.005	150	15
7	3.0	50	2.8	110	8	0.474 ± 0.005	162	15
8	6.4	40	1.6	90	5	1.29 ± 0.03	252	10
9	12.4	40	3.4	100	5	2.5 ± 0.1	279	5

TABLE 2. Experimental parameters for five laboratory experiments in which a monopolar vortex was submitted to a strain flow. Before the onset of the vortex generation, the ambient flow was allowed to develop during a time period t_f. The other symbols are defined in the text.

The relationship appears to be close to linear in the core of the vortex, but highly nonlinear in the outer region of the vortex.

Detailed laboratory observations by Trieling & van Heijst (1997) revealed that the radial expansion of the vortex can mainly be ascribed to horizontal diffusion of vorticity and can be expressed analytically as

$$r_m^2 = r_0^2 + 2\nu t, \tag{4.5}$$

where r_0 represents the radius of the peak velocity at $t = 0$. In their study, it was also shown that the decay of maximum vorticity near the mid-plane ($z = 0$) can be accurately described by the relation

$$\omega_m = \frac{C}{\nu^{5/2} t^{1/2} (t + t_0)^2}, \tag{4.6}$$

in which C is a constant and the 'initial time' t_0 is related to the initial radius of the vortex by $r_0 = (2\nu t_0)^{1/2}$. A simple scaling analysis by Flór & van Heijst (1996) demonstrated that the decay of (maximum) vorticity is mainly caused by vertical diffusion of vorticity.

5. Observed behaviour of a monopolar vortex in a strain flow

The typical observed evolution of a monopolar vortex in a strain flow is illustrated by the vorticity contour plots in figure 10. The main experimental parameters are listed in table 2 for five different experiments. In this case, experiment 6, the strain rate was equal to 0.303×10^{-2} s^{-1}. Figure 10 (*a*) shows the vorticity contours 60 s after the generation of the vortex. It can be clearly seen that the vortex is still approximately circular and has a core of positive vorticity surrounded by a ring of negative vorticity. In the next stage, see (*b*) and (*c*), this ring breaks up into two patches, positioned at an angle of approximately 45° with respect to the horizontal strain axis, which are soon thereafter removed from the vortex core by the ambient flow, see (*d*). Eventually, the core of positive vorticity remains, surrounded by weak oppositely signed vorticity, as evident from (*e*) and (*f*). Comparison of frames (*d*)–(*g*) reveals that the vortex elongates, while at high vorticity values, its orientation remains almost constant at an angle of 45° with respect to the horizontal strain axis. In the final stage, beyond $t \approx 600$ s (see *h*), the elliptic-like vortex rotates towards the horizontal strain axis and is continuously elongated by the ambient flow. Note that during the total time evolution, the vortex expands while decaying owing to diffusion of vorticity in radial and vertical directions.

https://doi.org/10.1017/S0022112097006356 Published online by Cambridge University Press

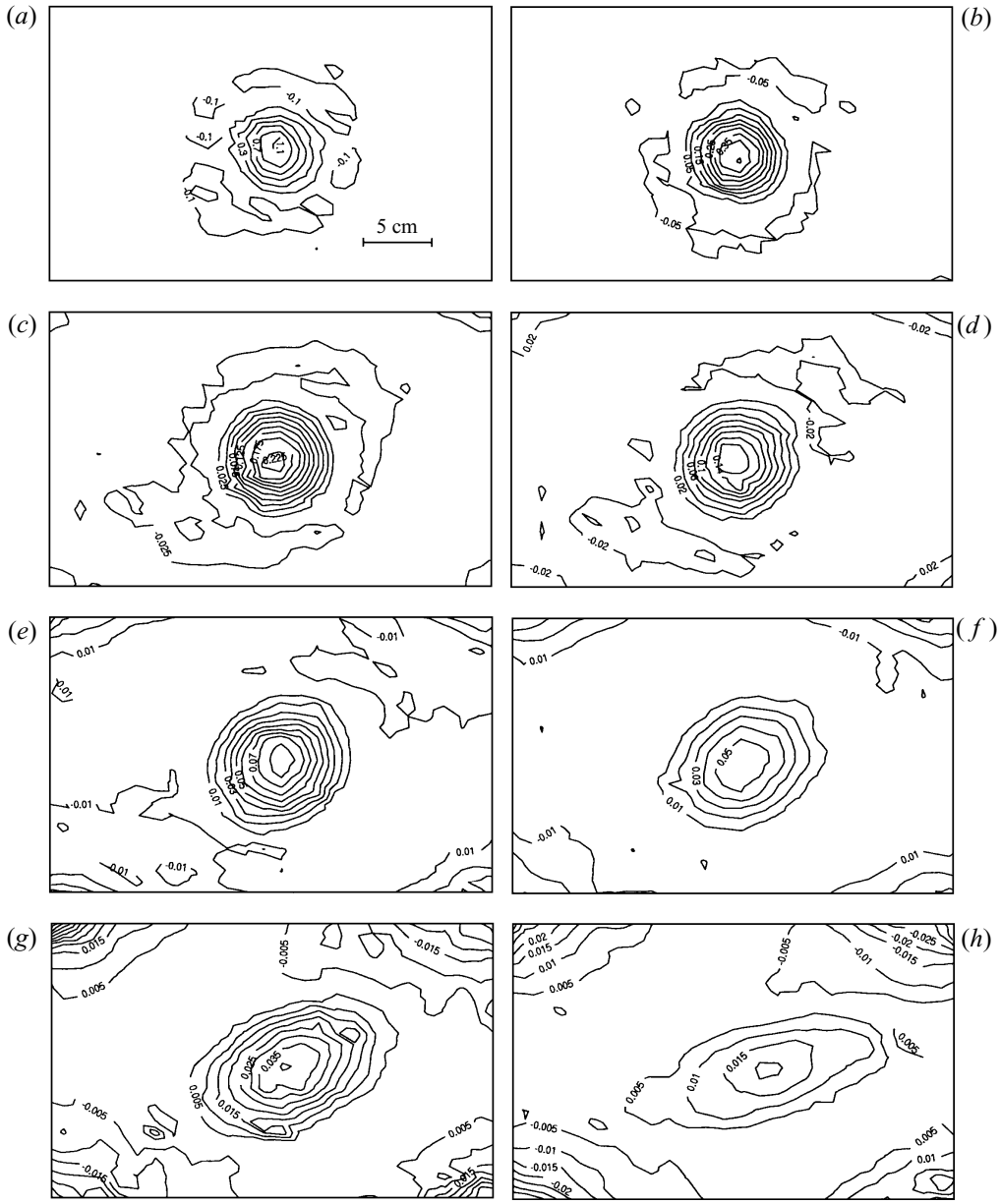


FIGURE 10. Contour plots of vorticity ω for a monopolar vortex in a strain flow of (initial) strength $e = 0.303 \times 10^{-2}$ s^{-1}: (*a*) $t = 60$ s, (*b*) 120 s, (*c*) 180 s, (*d*) 240 s, (*e*) 360 s, (*f*) 480 s, (*g*) 600 s and (*h*) 840 s. The contour labels are given in units of s^{-1}. Experimental parameters are given in table 2 (experiment 6).

The strain rate dependence of the vortex evolution was examined by performing similar experiments to those shown in figure 10, but with higher strain rates. The effect of the larger strain rate $e = 0.474 \times 10^{-2}$ s^{-1} (experiment 7) is evident from the vorticity plots presented in figure 11 (*a–h*). The rotation speed and the forcing period of the sphere were taken approximately the same as in the previous experiment. At $t = 75$ s, (*a*), the core of the vortex is circular, but the accompanying negative

https://doi.org/10.1017/S0022112097006356 Published online by Cambridge University Press

vorticity is already concentrated into two satellites, which are located on opposite sides of the vortex core. When both patches of negative vorticity are orientated at an angle of approximately 45° with respect to the horizontal strain axis, as observed in (*b*), they are quickly advected by the strain flow, see (*c*), and an elliptic vortex remains with mainly positive vorticity, as shown in (*d*). After $t \approx 375$ s, both the fast elongation and the overturning motion of the vortex are clearly visible from (*e*)–(*g*). Finally, the vortex is completely torn apart along the horizontal strain axis, and the basic strain flow remains, as can be seen in (*h*). Comparison with figure 10 reveals that the indefinite elongation of the vortex sets in sooner when a larger strain rate is applied.

Figure 12 shows the evolution of a monopolar vortex in a strain flow of strength $e = 2.5 \times 10^{-2}$ s^{-1} (experiment 9), which is considerably stronger than the strain rates related to figures 10 and 11. In order to minimize the effect of the ambient flow on the vortex generation, the sphere was spun for a shorter time period and with a higher rotation speed. Almost immediately after the generation of the vortex, the ring of negative vorticity is carried away by the ambient flow, as can be observed in figure 12 (*a, b*). Likewise, the irreversible elongation of the vortex has already started at $t \approx 160$ s, see (*c*)–(*f*), which is much sooner than for weaker strain rates. Nevertheless, a similar evolution is observed as in figures 10 and 11. Therefore, it can be concluded that the strain rate merely determines the speed of the vortex evolution, but not the evolution itself.

The shedding of the negative vorticity ring can be explained by considering the stream function plots, which are depicted in figure 11 (*a′*–*h′*). Two types of streamlines can be defined for these graphs: 'closed' streamlines, which enclose the centre of the vortex, and 'open' streamlines, which are apparently unbounded (actually each encloses one of the rotating discs). Both types are separated by the so-called 'separatrix', which is the boundary of the nested set of closed streamlines. In most plots two stagnation points can be identified, which both lie on the separatrix, provided that the flow is symmetric with respect to both strain axes. If the flow is stationary, fluid particles within the separatrix are trapped and rotate around the vortex centre, whereas outside they follow unbounded trajectories. However, owing to the decay of vorticity, the area enclosed by the separatrix becomes smaller, i.e. fluid particles that were initially trapped are forced to leave the enclosed region. Furthermore, horizontal diffusion may account for a continuous leakage of vorticity through the separatrix. Nevertheless, as will be shown later on, the vortex core evolves in a quasi-stationary fashion until it is torn apart indefinitely by the ambient flow. Therefore, inside the separatrix, material lines will be very close to streamlines.

At $t = 75$ s (see figure 11 *a, a′*) the vortex is almost entirely enclosed by the separatrix. However, as time increases, negative vorticity leaks through the separatrix owing to the processes described above. The fluid being expelled contains only low-amplitude vorticity and will therefore be advected very much like a passive scalar. Accordingly, negative vorticity accumulates near the stagnation points, see (*b, b′*), giving rise to two patches of negative vorticity which are carried away along the open streamlines, as shown in (*c, c′*). Next, low-amplitude positive vorticity crosses the separatrix, as can be inferred from (*d, d′*) and (*e, e′*), which will also be advected towards the stagnation points. Note that until this stage, the vorticity contours inside the separatrix closely match the corresponding streamlines. Soon thereafter, however, the area enclosed by the separatrix quickly decreases (see *f′*), the stagnation points vanish (see *g′*) and the basic strain flow pattern returns, as can be observed in (*h′*). As a result, the entire vortex structure rotates towards the horizontal strain axis and

https://doi.org/10.1017/S0022112097006356 Published online by Cambridge University Press

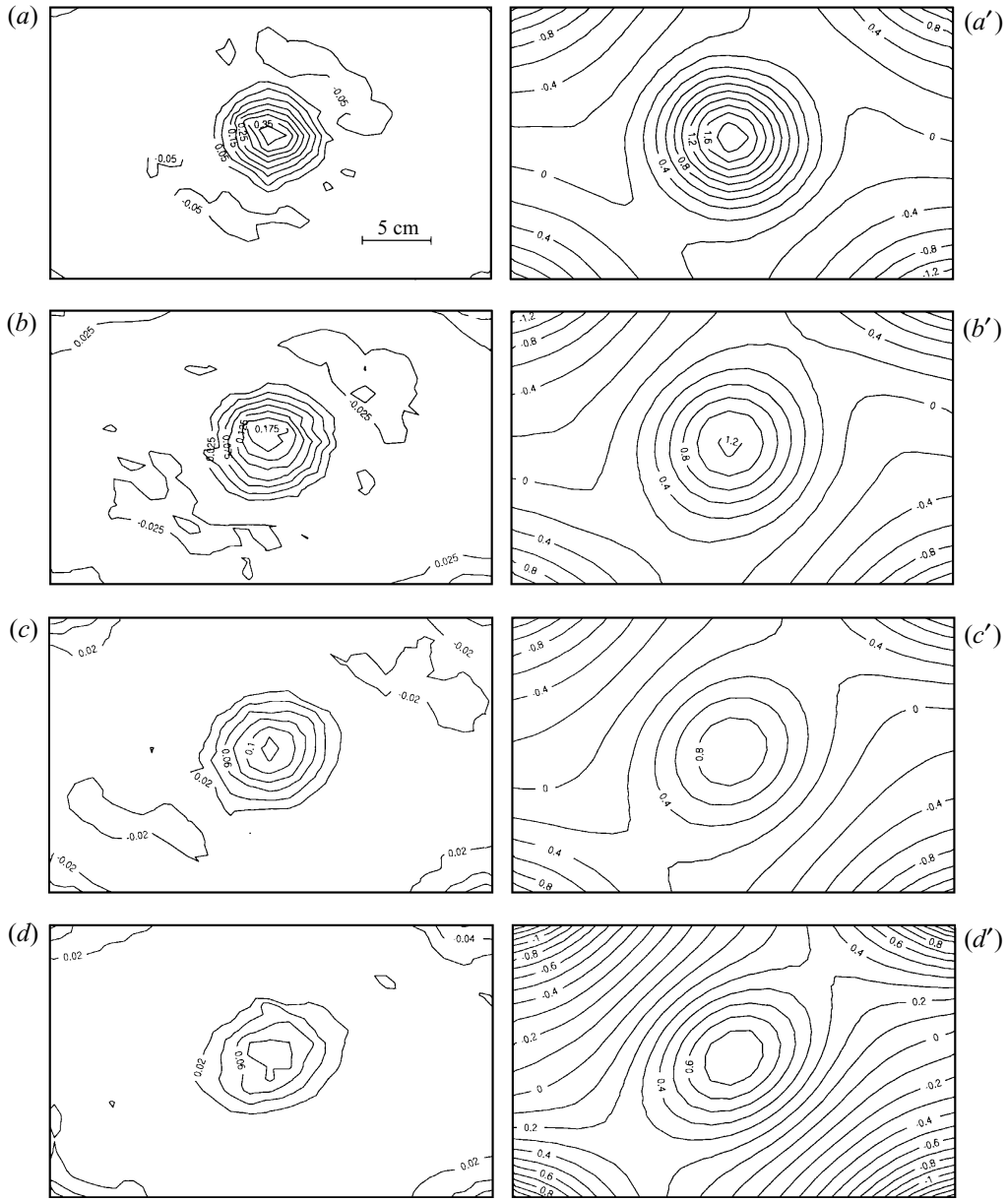


FIGURE 11 (*a–d* and *a′–d′*). For caption see facing page.

the indefinite vortex elongation sets in (see *f–h*). Similar streamline patterns were obtained for other experiments (see e.g. figure 12 *a′–f′*).

The advection of negative vorticity can be illustrated differently by plotting the vorticity ω and the velocity component v along the x-axis, as shown in figure 13 (experiment 6). The measured data points (indicated by squares) were obtained from the values at the grid points by bilinear interpolation. The vorticity and velocity have been scaled with their extremal values ω_m and v_m, respectively, whereas the x-coordinate has been scaled with the position of the peak velocity. The observed

https://doi.org/10.1017/S0022112097006356 Published online by Cambridge University Press

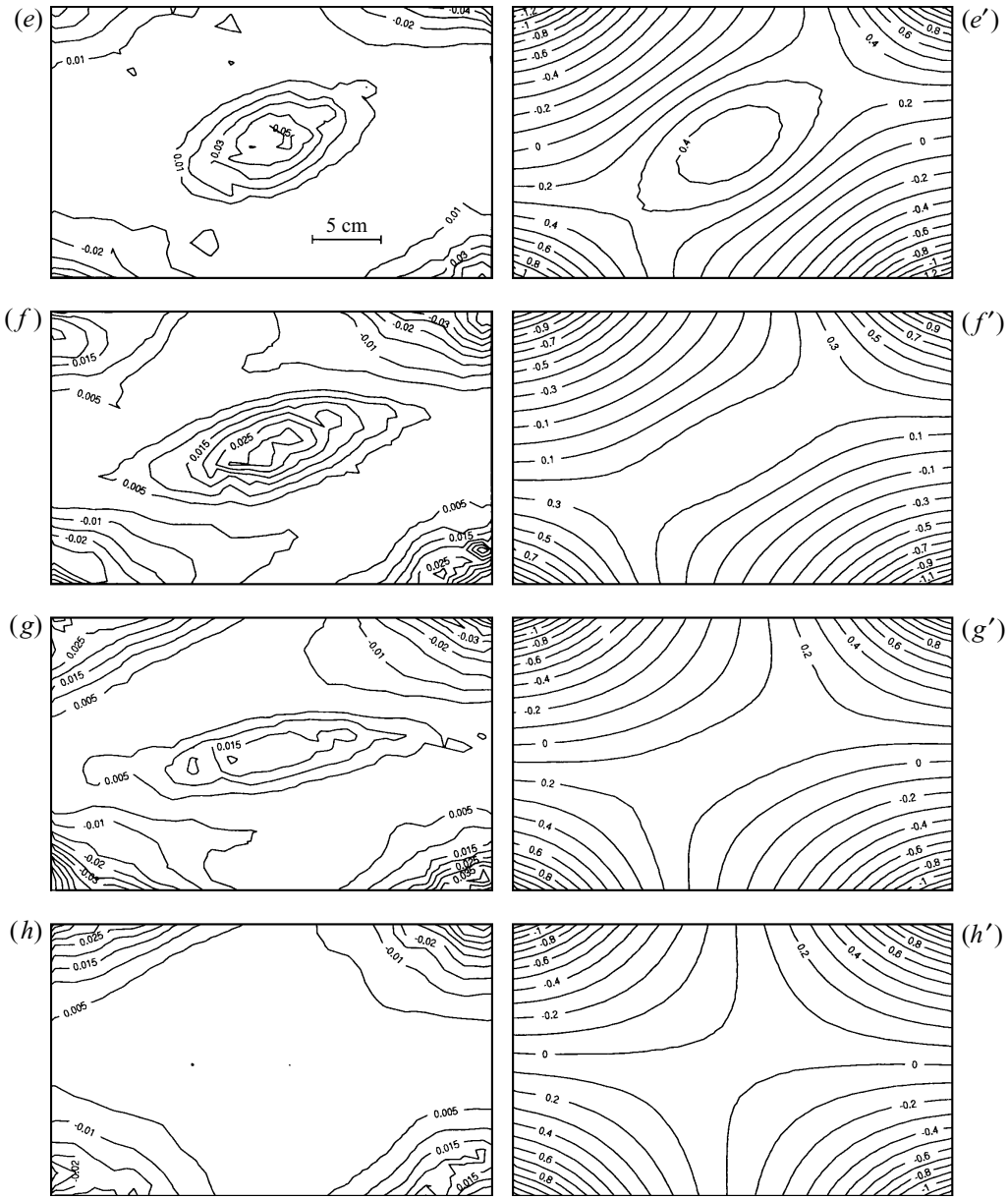


FIGURE 11. Contour plots of vorticity ω (left column) and corresponding stream function ψ (right column) for a monopolar vortex in a strain flow with (initial) strength $e = 0.474 \times 10^{-2}$ s^{-1}: (a, a') $t = 75$ s, (b, b') 135 s, (c, c') 195 s, (d, d') 255 s, (e, e') 375 s, (f, f') 495 s, (g, g') 615 s and (h, h') 855 s. The vorticity and stream function values are given in units of s^{-1} and cm^2 s^{-1}, respectively. Experimental parameters are given in table 2 (experiment 7).

data are compared with the self-similar profiles (4.1) and (4.2) associated with the Gaussian vortex model (solid lines). In figure 13 (*a*), the measured cross-sectional vorticity distribution is shown at $t = 120$ s. Obviously, the vortex core is surrounded by a well-defined ring of negative vorticity, and the measured data are in good agreement with the Gaussian vortex model. However, at $t = 360$ s (see *c*), the (scaled)

https://doi.org/10.1017/S0022112097006356 Published online by Cambridge University Press

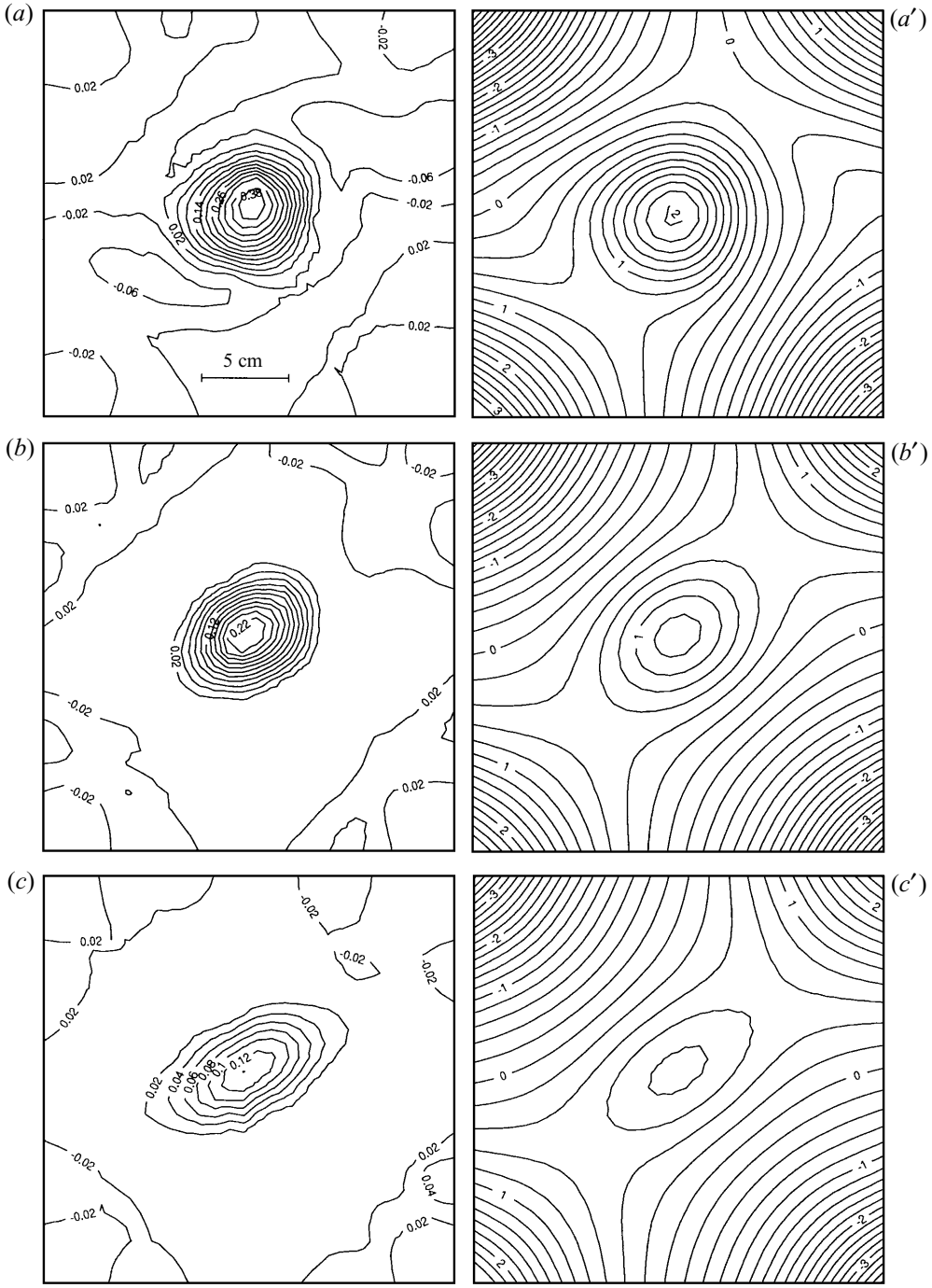


FIGURE 12(*a–c* and *a′–c′*). For caption see facing page.

amplitude of the negative vorticity has decreased by a factor 2, whereas the core of the vortex still closely matches the profile corresponding to the Gaussian vortex model. In this case, part of the negative vorticity has been removed from the vortex along the open streamlines.

https://doi.org/10.1017/S0022112097006356 Published online by Cambridge University Press

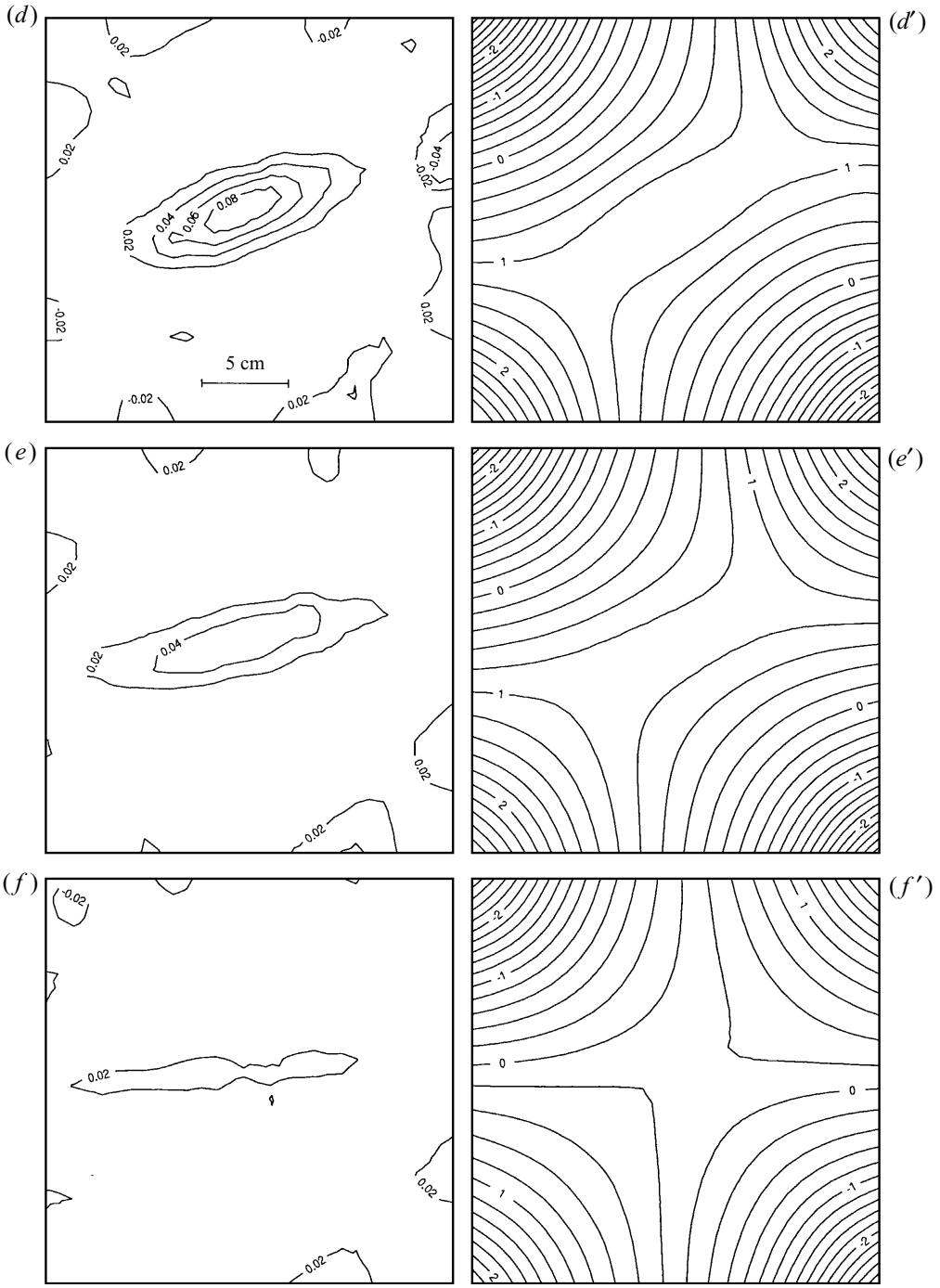


FIGURE 12. Contour plots of vorticity ω (left column) and corresponding stream function ψ (right column) for a monopolar vortex in a strain flow with $e \approx 0.025\ \mathrm{s}^{-1}$: (a, a') $t = 40$ s, (b, b') 120 s, (c, c') 180 s, (d, d') 220 s, (e, e') 260 s and (f, f') 320 s. The vorticity and stream function values are given in units of s^{-1} and $\mathrm{cm}^2\,\mathrm{s}^{-1}$, respectively. Experimental parameters are given in table 2 (experiment 9).

https://doi.org/10.1017/S0022112097006356 Published online by Cambridge University Press

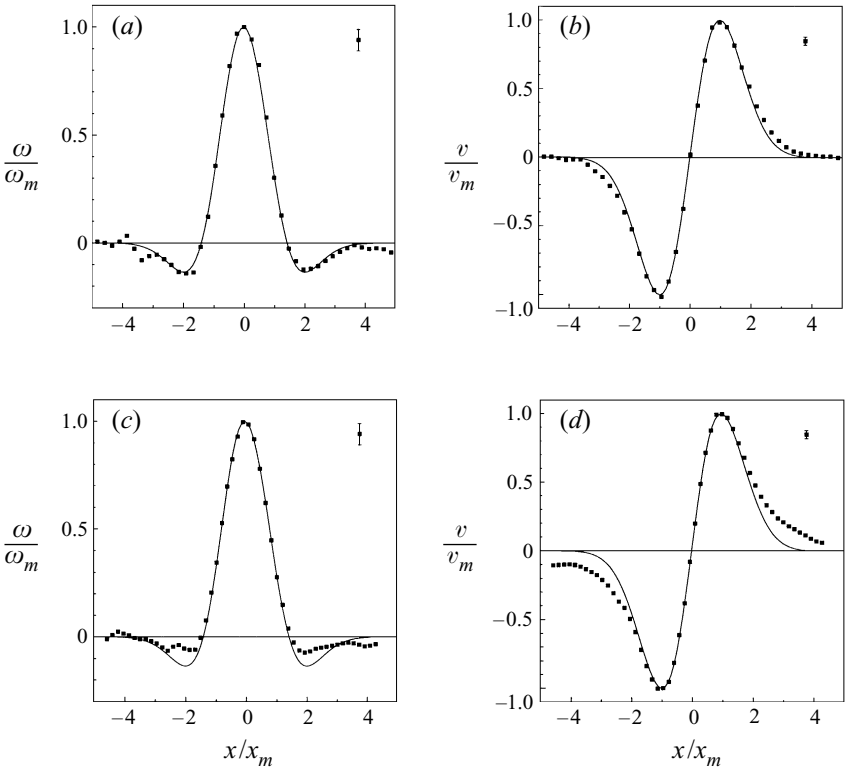


FIGURE 13. Cross-sectional distributions of the vorticity ω (left column) and the velocity component v (right column) along the x-axis at (a,b) $t = 120$ s and (c,d) 360 s, for a monopolar vortex in a strain flow. The vorticity and velocity have been scaled with their extremal values ω_m and v_m, respectively, whereas the x-coordinate has been scaled with the position of the peak velocity x_m. The observed data (denoted by squares) are compared with the profiles corresponding to the Gaussian vortex (solid lines). At $t = 120$ s: $\omega_m = 0.41\ \mathrm{s}^{-1}$, $v_m = 0.40\ \mathrm{cm\,s}^{-1}$ and $r_m = 2.9$ cm; whereas at $t = 360$ s: $\omega_m = 0.09\ \mathrm{s}^{-1}$, $v_m = 0.11\ \mathrm{cm\,s}^{-1}$ and $r_m = 4.0$ cm. Experimental parameters: see table 2 (experiment 6).

The removal of negative vorticity is also evident from the accompanying velocity profiles depicted in figure 13 (b,d). Initially, the measured velocity data are in good agreement with the Gaussian vortex model, as shown in figure 13 (b), but later on, see figure 13 (d), the tail of the observed velocity profile becomes less steep and tends towards a $1/r$-velocity distribution, indicating that vorticity has been carried away by the ambient flow.

In summary, the results in figures 11–13 show that outside the separatrix vorticity is being removed from the vortex, whereas inside the separatrix the cross-sectional distribution of vorticity remains self-similar in time. Hence, the separatrix serves as a sharp boundary between the inner and outer flow.

Close observation of figures 11 and 12 reveals that the vorticity contours in the core of the vortex coincide closely with the corresponding streamlines for a considerable time until the vortex is overcome by the strain flow. Stationary vortices are characterized by a functional relationship between vorticity ω and stream function ψ, and therefore it is argued that the initial evolution of the observed vortex in the straining field is quasi-stationary. To obtain a more quantitative idea of this process, the vorticity has been plotted versus the stream function in a scatter plot for four

https://doi.org/10.1017/S0022112097006356 Published online by Cambridge University Press

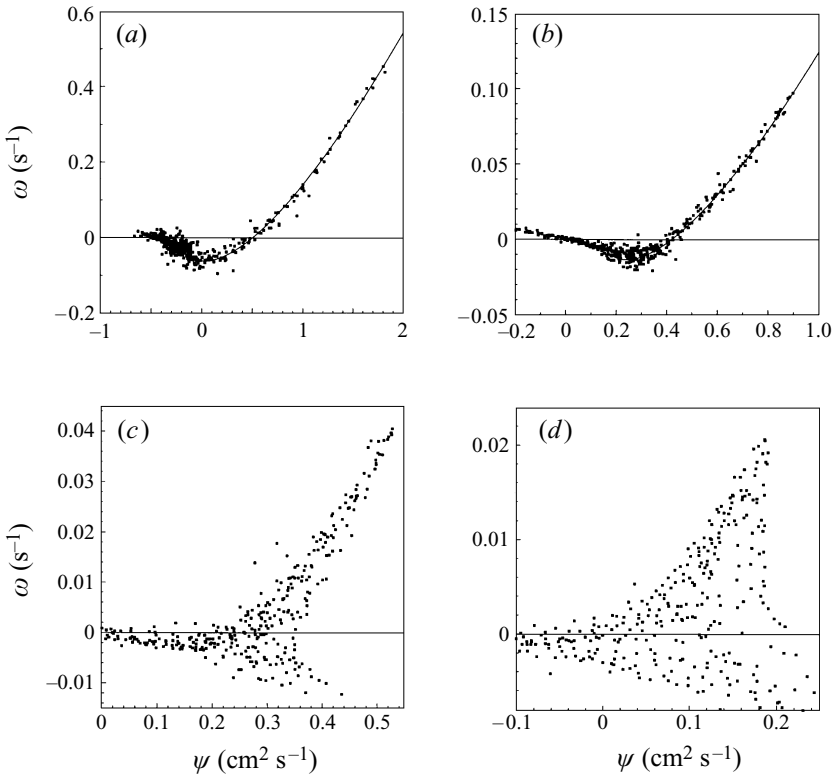


FIGURE 14. Sequence of measured (ω, ψ)-scatter plots (squares) showing the typical evolution of the (ω, ψ)-relation for a monopolar vortex in a strain flow: (*a*) $t = 120$ s, (*b*) 360 s, (*c*) 600 s and (*d*) 840 s. In (*a*) and (*b*), the (ω, ψ)-relationship (4.4) of the Gaussian vortex (solid line) has been least-square fitted to the observed data for $\omega > 0.25\omega_m$. Experimental parameters: see table 2 (experiment 6).

successive times (see figure 14). For clarity, the background vorticity close to the rotating discs has been excluded. Figure 14 (*a*) shows the scatter plot at $t = 120$ s, and a good agreement is obtained with the (ω, ψ)-relationship of a Gaussian vortex (solid line), which has been fitted with the experimental data for $\omega > 0.25\omega_m$. So far, the main vortex characteristics appear to be not affected by the strain flow. However, at $t = 360$ s (see *b*), the scatter in the vortex ring is more pronounced, because negative vorticity is being shed from the vortex by the strain flow. At this time, the positive branch is still virtually unaffected. After that, low-amplitude vorticity of positive sign is carried away by the ambient flow, which is obvious in (*c*) ($t = 600$ s) from the scatter in the positive vorticity branch. Note that the scatter is less pronounced for larger values of positive vorticity, which implies that the main part of the vortex core is still close to equilibrium. Finally, the vortex rotates towards the horizontal strain axis while simultaneously being torn apart, as evident on (*d*) ($t = 840$ s) from the large scatter in the entire vortex. Based on these scatter plots it can be concluded that the main part of the vortex core evolves in a quasi-stationary manner until the vortex is overcome by the strain flow. A similar quasi-stationary behaviour has been observed in numerical studies by Legras & Dritschel (1993, 1994) and Dritschel (1995).

At high vorticity amplitudes, the vorticity contours have a shape that is close

https://doi.org/10.1017/S0022112097006356 Published online by Cambridge University Press

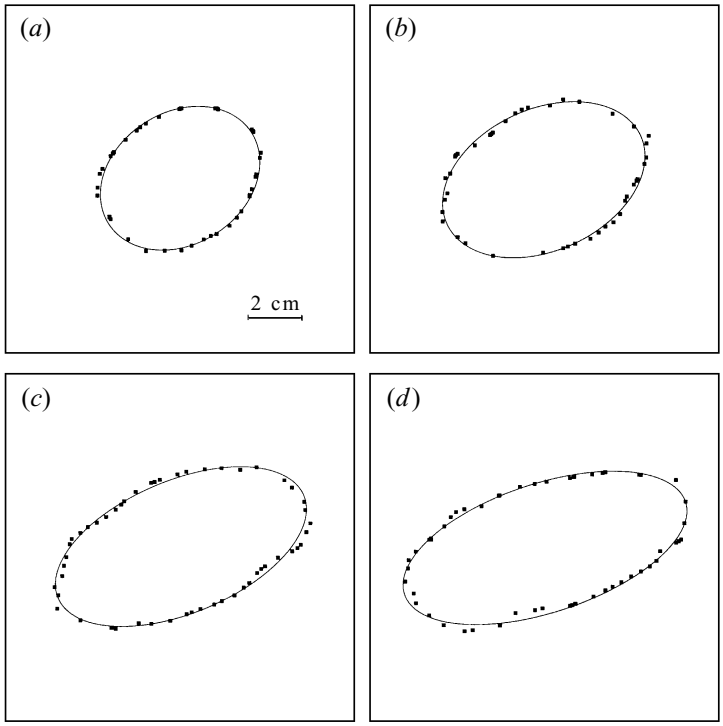


FIGURE 15. Typical discretized vorticity contours $\omega = 0.607\omega_m$ of a vortex in a strain flow at four different times: (*a*) $t = 420$ s, (*b*) 600 s, (*c*) 720 s and (*d*) 840 s. A perfect elliptic contour (solid line) has been been fitted to each measured contour. Experimental parameters: see table 2 (experiment 6).

to elliptic, as can be seen in figures 10–12. In figure 15, typical measured vorticity contours are shown, which are represented by the squares. A least-squares algorithm was used to fit each observed contour with an ellipse (solid line), and a good agreement is obtained in each case. This procedure was applied to several vorticity contours and their corresponding streamlines at various moments of time. In this way, aspect ratios $\lambda_\omega(\omega, t)$ and $\lambda_\psi(\psi, t)$, and orientations $\phi_\omega(\omega, t)$ and $\phi_\psi(\psi, t)$ were obtained. The relative error in these quantities is estimated to be less than 5%, provided that the corresponding contours are not too close to circular. The temporal evolution of λ_ω and ϕ_ω will be given in the next section.

A similar method, introduced by Overman & Zabusky (1984), has been applied to numerical simulations by Melander, McWilliams & Zabusky (1987). The latter authors determined the aspect ratio and orientation of an elliptic-like contour by calculating the second-order moments of the domain contained by that specific contour. Because of the relatively low resolution of the present laboratory observations, however, this approach was not adopted here, and the simple least-squares algorithm appeared to be the most suitable method.

In the region inside the separatrix, both $\lambda_\omega(\omega, t)$ and $\phi_\omega(\omega, t)$ varied by less than 10% as a function of ω, which was also true for the aspect ratio and orientation of the stream function contours. In other words, $\lambda_\omega(\omega, t) \approx \lambda_\omega(t)$ and $\phi_\omega(\omega, t) \approx \phi_\omega(t)$, and likewise for the aspect ratio and orientation of the closed streamlines. Obviously, the vortex core is robust and in this respect shows much resemblance with an elliptic patch of uniform vorticity. Although the laboratory vortex has a continuous spatial

https://doi.org/10.1017/S0022112097006356 Published online by Cambridge University Press

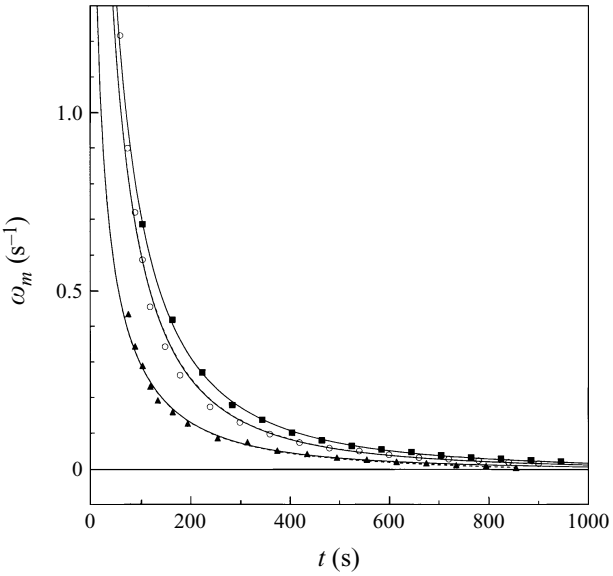


FIGURE 16. Temporal evolution of the peak vorticity ω_m for a monopolar vortex in a strain flow: $e = 0$ s^{-1} (experiment 5, squares), $e = 0.303\times10^{-2}$ s^{-1} (experiment 6, circles) and $e = 0.474\times10^{-2}$ s^{-1} (experiment 7, triangles). The observed data have been least-square fitted by (4.6) (solid lines), which yielded the following values for the constant C and the initial age t_0 (with $\nu = 1.065\times10^{-2}$ cm^2 s^{-1}): $C = 11.2$ cm^5 s^{-1}, $t_0 = 263$ s (experiment 5); $C = 7.7$ cm^5 s^{-1}, $t_0 = 227$ s (for $t < 700$ s, experiment 6); $C = 5.0$ cm^5 s^{-1}, $t_0 = 279$ s (for $t < 400$ s, experiment 7). The mean errors in C and t_0 were 0.7 cm^5 s^{-1} and 24 s, respectively. The dashed lines (which closely follow the solid lines) correspond to the numerically obtained decay of maximum vorticity (see § 6).

vorticity distribution, it will be demonstrated in the next section that its core shows similar behaviour to an elliptic patch of uniform vorticity in a background strain flow.

During the initial quasi-stationary evolution of the vortex, also $\lambda_\omega(t) \approx \lambda_\psi(t)$ and $\phi_\omega(t) \approx \phi_\psi(t)$, i.e. the contours are in phase (see figures 11 *d* and 11 *d*′ as an example). However, when the vortex starts to tumble towards the horizontal strain axis, the equivorticity lines and streamlines inside the separatrix become phase shifted, i.e. $\phi_\omega(t) < \phi_\psi(t)$. For instance, compare the orientation of the vorticity contours and streamlines plotted in figures 11 (*f*) and 11 (*f*′), respectively. The reason for this phase shift is that the streamline pattern is rather insensitive to the exact shape of the vortex.

In figure 16, the temporal decay of maximum vorticity ω_m is plotted for the experiments shown in figure 10 (circles, experiment 6) and figure 11 (triangles, experiment 7). Also, the decay of the peak vorticity is presented for a vortex without background flow (squares, experiment 5). In these three experiments, both the rotation speed and the forcing period of the sphere were taken approximately the same. Each data set was least-square fitted by (4.6), where the constant C and the initial time t_0 were taken as free parameters. In a numerical study by Mariotti, Legras & Dritschel (1994) on monopolar vortices in shear flows, it was observed that during the final stage of indefinite elongation the decay of maximum vorticity accelerates through the combined effect of shear and horizontal diffusion. Since their numerical results may also be applied to the case of a monopolar vortex in a strain flow, in figure 16 only the initial stage of the maximum vorticity evolution was least-squares fitted, i.e. $t < 700$ s for experiment 6 and $t < 400$ s for experiment 7. Although relation (4.6)

https://doi.org/10.1017/S0022112097006356 Published online by Cambridge University Press

has been derived for a Gaussian vortex in still ambient fluid, for each experiment a good agreement is obtained until the moment of indefinite elongation. Apparently, the functional decay of maximum vorticity is not affected by the strain flow until the final stage of the evolution. In the next section, this assertion will be confirmed by numerical simulations.

Nevertheless, it is clear from figure 16 that at each moment of time the peak vorticity is smaller for larger strain rates, although in each experiment the vortex was generated with approximately the same rotation speed and forcing period. Therefore, it is most likely that the formation of the vortex is affected by the strain flow: during the spinning of the sphere, fluid is swept away horizontally near the sphere's equator, so that part of the momentum might be removed by the background flow before a well-defined vortex is formed, with less momentum, i.e. weaker maximum vorticity, than for a vortex in still ambient fluid.

6. Modelling of monopolar vortices in a strain flow

Only a few exact solutions of the two-dimensional Euler equations are known concerning the motion of elliptic vortices. It was shown analytically by Kirchhoff (1876) that an elliptic patch of uniform vorticity in an otherwise quiescent fluid rotates steadily around its centre, without any shape changes. Likewise, steady elliptic vortices in a uniform shear flow were considered by Moore & Saffman (1971), whereas the corresponding unsteady solutions were obtained by Kida (1981). Since a uniform shear flow can be decomposed into a solid-body rotation and a pure strain flow, Kida's analysis can be applied to the case of a vortex in a pure strain flow.

The laboratory observations presented in § 5 have demonstrated that the vortex core bears much resemblance to an elliptic patch of uniform vorticity as far as the shape of the vorticity contours is concerned. Therefore, as a first approach, the laboratory vortex will be modelled by an elliptic patch of uniform vorticity, and Kida's original model will be extended to account for the observed decay of vorticity. It will be shown that during the initial stage, the vortex patch evolves close to equilibrium states, just like observed in the laboratory.

As a second approach, the full two-dimensional vorticity equation will be solved numerically by a finite-difference method to account for the non-uniform vorticity distribution of the laboratory vortex and the horizontal diffusion of vorticity. The results will be compared with the laboratory observations.

6.1. *Motion of a uniform elliptic vortex in a pure strain flow*

An elliptic region of uniform vorticity ω_0 is considered with aspect ratio λ and with its major axis tilted by an angle ϕ with respect to the x-axis. The vortex is embedded in a pure strain flow, for which the velocity components in the Cartesian directions (x, y) are given by (3.1).

According to Kida (1981), the equations of motion for the elliptic vortex are given by

$$\dot{\lambda} = 2e\lambda \cos 2\phi, \tag{6.1}$$

$$\dot{\phi} = -e\frac{\lambda^2 + 1}{\lambda^2 - 1} \sin 2\phi + \frac{\omega_0 \lambda}{(\lambda + 1)^2}, \tag{6.2}$$

where e represents the strain rate, and differentiation with respect to time is denoted by a dot.

https://doi.org/10.1017/S0022112097006356 Published online by Cambridge University Press

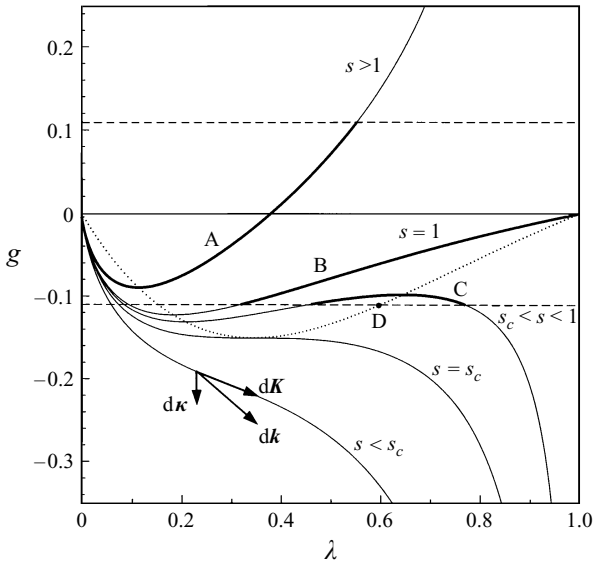


FIGURE 17. Graph showing the g-function versus λ for different values of s (indicated by the solid lines) in the case of a pure strain flow. The local extrema of g are connected by the dotted line. The heavy solid lines, which are bounded by the extremal values $g = \pm\Lambda = \pm 0.11$ (dashed lines), represent different kinds of motion of the elliptic vortex: irreversible elongation (A), rotation (B), nutation (C) and equilibrium (D). Also the vector decomposition of $\mathrm{d}\boldsymbol{k}$ is indicated for a time-dependent Λ (see text).

From (6.1) and (6.2) several types of motion can be derived depending on the ratio $\Lambda = |e/\omega_0|$ as well as the initial aspect ratio λ_0 and orientation ϕ_0 of the elliptic vortex. When the rate of strain is larger than a critical value, i.e. $\Lambda > \Lambda_c = 0.150$†, the vortex will be elongated irreversibly in the strain direction, whereas in weaker strain flows ($\Lambda < \Lambda_c$) the vortex may rotate around its centre or wobble around a fixed angle, generally with shape oscillations. For each value of $\Lambda < \Lambda_c$, two stationary states exist, of which one is unstable. These steady solutions have also been obtained before by Moore & Saffman (1971).

Following Kida, the occurrence of these different types of motion may be explained qualitatively by combining (6.1) and (6.2), which yields

$$\frac{e}{\omega_0}\sin 2\phi = g(\lambda; s), \tag{6.3}$$

where the function g is defined by

$$g(\lambda; s) \equiv \frac{\lambda}{\lambda^2 - 1}\ln\frac{(\lambda+1)^2}{4s\lambda}, \tag{6.4}$$

with s a constant of integration. Differentiation of (6.4) with respect to λ, and using (6.2), leads to

$$\dot{\phi} = \omega_0\lambda\left.\frac{\partial g}{\partial\lambda}\right|_s, \tag{6.5}$$

implying that the rotation of the vortex is related to the derivative of g with respect to λ.

† The numerical values presented in this section are accurate to within one unit in the last digit.

https://doi.org/10.1017/S0022112097006356 Published online by Cambridge University Press

Now, the motion of the elliptic vortex can be deduced by considering the family of g-functions plotted in figure 17, where each curve corresponds to a particular value of s. Since $g(\lambda;s) = -g(1/\lambda;s)$ and the equations of motion are invariant under the transformation $(\omega_0, \phi) \rightarrow (-\omega_0, -\phi)$, it suffices to consider the range $0 \leqslant \lambda \leqslant 1$ and $\omega_0 \geqslant 0$. If $0 < s \leqslant s_c$, with s_c ($= 0.893$) a critical value, g is a monotonically decreasing function of λ, while it has two extremal values if $s_c < s < 1$. Only one extremal value is present for $s \geqslant 1$. When $s = s_c$, the two extremal values coincide at $\lambda = \lambda_c = 0.346$, for which $g = -\Lambda_c = -0.150$. In figure 17, the (local) extremal values are connected by the dotted line.

The state of the elliptic vortex is given by (λ, ϕ), which can be represented in the (λ, g)-plane (figure 17) by the vector $\boldsymbol{k}$, defined by

$$\boldsymbol{k} \equiv (\lambda, g), \tag{6.6}$$

where g merely represents the orientation ϕ of the vortex, as can be seen from relation (6.3). (Here, the vector $\boldsymbol{k}$ should not be confused with the unit vector introduced in § 2.) For example, a circular-shaped vortex corresponds to $\boldsymbol{k} = (1, 0)$, whereas an infinitely elongated vortex is represented by $\boldsymbol{k} = (0, 0)$. Strictly speaking, $\boldsymbol{k}$ represents two degenerate states in the (λ, g)-plane that have the same aspect ratio but different orientations, i.e. (λ, ϕ) and $(\lambda, \pi/2 - \phi)$. However, the actual state is always obvious from the sign of $\dot{\lambda}$ in (6.1).

Likewise, the motion of the vortex, represented by $(\dot{\lambda}, \dot{\phi})$, is given in the (λ, g)-plane by

$$\frac{\mathrm{d}\boldsymbol{k}}{\mathrm{d}t} = (\dot{\lambda}, \dot{g}). \tag{6.7}$$

Note that $\dot{g}$ is related to $\dot{\phi}$ through relation (6.5), since $\dot{g} = (\partial g/\partial \lambda)|_s \dot{\lambda}$.

Given a value for the constant s, which is determined by the initial state $\boldsymbol{k}_0$, i.e. (λ_0, ϕ_0), the vector $\boldsymbol{k}$ moves along the corresponding g-curve, where the direction of motion (along the λ-axis) is determined by (6.1). From (6.3) it follows that the motion in the (λ, g)-plane is restricted to the region $|g| \leqslant \Lambda$. When $|g| = \Lambda$, the motion of the vortex is reversed by (6.1), i.e. $\dot{\lambda} = 0$. It is this restriction that brings about the different types of motion. This is illustrated by the marked g-curves in figure 17, where $\Lambda = 0.11$ is taken as an example. Curve A corresponds to a vortex that will eventually be elongated along the horizontal strain axis, while curve B represents a rotating vortex (note that this curve continues into the region $\lambda > 1$). Curve C indicates a vortex that oscillates around a fixed angle, and point D represents a stationary vortex, i.e. $\dot{\lambda} = 0$ and $\dot{\phi} = 0$.

6.1.1. *Decay of vorticity*

In order to model the observed decay of vorticity associated with the dominating vertical diffusion, Kida's original model will be extended by allowing the uniform vorticity of the vortex patch to decrease in time according to some prescribed function $\omega_0(t)$. Laboratory observations presented in § 5 have shown that the time evolution of (maximum) vorticity is not affected significantly by the strain flow. Therefore, the decay of uniform vorticity will be modelled by (4.6) corresponding to a Gaussian vortex without background flow. It should be stressed that the extended vortex patch model only allows for the vertical diffusion of vorticity, whereas horizontal diffusion is not accounted for, i.e. the horizontal vorticity distribution of the vortex patch remains uniform.

When the uniform vorticity of the elliptic vortex patch is allowed to decay in time

https://doi.org/10.1017/S0022112097006356 Published online by Cambridge University Press

as described above, the foregoing analysis is still applicable, but now the parameters ω_0 and s are functions of time, i.e. $\omega_0 = \omega_0(t)$ and $s = s(t)$. For each time, the state and the motion of the vortex in the (λ, g)-plane are represented again by the vectors $\boldsymbol{k}$ and $\mathrm{d}\boldsymbol{k}/\mathrm{d}t$, respectively. However, the motion is no longer restricted to g-curves of constant s, which can be seen as follows. By defining

$$h(\phi;\omega_0) \equiv \frac{e}{\omega_0}\sin 2\phi, \tag{6.8}$$

expression (6.3) can be written as

$$g(\lambda;s) = h(\phi;\omega_0). \tag{6.9}$$

Differentiation of g with respect to time yields

$$\begin{aligned} \dot{g} &= \dot{h} \\ &= \left.\frac{\partial h}{\partial \phi}\right|_{\omega_0}\dot{\phi} + \left.\frac{\partial h}{\partial \omega_0}\right|_{\phi}\dot{\omega}_0, \end{aligned} \tag{6.10}$$

so that the motion of the vortex is described by

$$\begin{aligned} \frac{\mathrm{d}\boldsymbol{k}}{\mathrm{d}t} &= \left(\dot{\lambda}, \left.\frac{\partial h}{\partial \phi}\right|_{\omega_0}\dot{\phi}\right) + \left(0, \left.\frac{\partial h}{\partial \omega_0}\right|_{\phi}\dot{\omega}_0\right) \\ &\equiv \frac{\mathrm{d}\boldsymbol{K}}{\mathrm{d}t} + \frac{\mathrm{d}\boldsymbol{\kappa}}{\mathrm{d}t}, \end{aligned} \tag{6.11}$$

where $\mathrm{d}\boldsymbol{K}/\mathrm{d}t$ corresponds to the motion of an elliptic patch with constant vorticity, and $\mathrm{d}\boldsymbol{\kappa}/\mathrm{d}t$ represents the motion due to the decay of vorticity.

The contribution from the decreasing vorticity can be rewritten as

$$\begin{aligned} \frac{\mathrm{d}\boldsymbol{\kappa}}{\mathrm{d}t} &= \left(0, -\frac{e\dot{\omega}_0}{\omega_0^2}\sin 2\phi\right) \\ &\equiv (0, \beta). \end{aligned} \tag{6.12}$$

Since $\dot{\omega}_0 < 0$ by assumption, it follows that

$$\begin{aligned} \beta > 0 \quad &\text{if} \quad g > 0, \\ \beta < 0 \quad &\text{if} \quad g < 0. \end{aligned}$$

Thus, the effect of the decaying vorticity is to shift the vector $\boldsymbol{k}$ to an adjoining upper or lower g-curve, depending on the sign of the original g-value. This is indicated schematically in figure 17.

6.1.2. *Non-uniform vorticity distribution*

In § 5 it was shown that the core of the laboratory vortex is characterized by the non-uniform vorticity distribution associated with the Gaussian vortex. It was also observed, however, that the vortex core has similar characteristics to an elliptic patch of uniform vorticity. Therefore, the laboratory observations will be compared with the extended Kida model by defining a mean vorticity value $\bar{\omega}$ for the laboratory vortex, according to

$$\bar{\omega}^* = \frac{1}{\pi}\int_0^{2\pi}\int_0^1 \omega^*(r^*)\, r^*\, \mathrm{d}r^*\, \mathrm{d}\phi, \tag{6.13}$$

where the vorticity distribution $\omega(r)$ has been scaled with its extremal value, and the radius r has been normalized by the corresponding radial position of the peak

https://doi.org/10.1017/S0022112097006356 Published online by Cambridge University Press

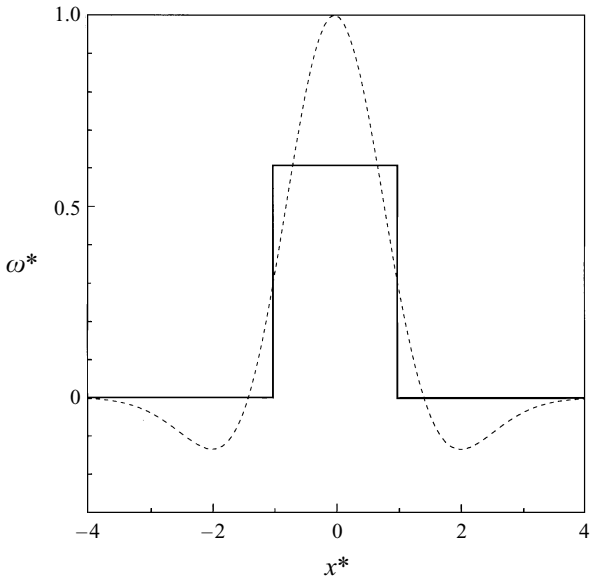


FIGURE 18. Vorticity profile of the Gaussian vortex (dashed line) compared with the uniform vorticity distribution of the vortex patch (solid line). The vorticity ω and spatial coordinate x have been normalized by the extremal vorticity ω_m of the Gaussian vortex and the corresponding radius of the peak velocity r_m, respectively.

velocity r_m. Since r_m is a convenient measure of the vortex core radius, only the region $r \leqslant r_m$ is considered to calculate the mean vorticity. When $\omega^*(r^*)$ is taken as the scaled vorticity distribution associated with the Gaussian vortex, see (4.1), it follows that $\bar{\omega}^* = 0.607$ (see figure 18).

Using (6.13) and $\bar{\omega}^* = 0.607$, the critical ratio between the rate of strain and the maximum vorticity can be calculated for a Gaussian vortex, according to

$$\left|\frac{e}{\omega_m}\right|_c = 0.607 \left|\frac{e}{\bar{\omega}}\right|_c = 0.607 \Lambda_c. \tag{6.14}$$

Since $\Lambda_c = 0.150$ it follows that $|e/\omega_m|_c = 0.091$. This is in good agreement with unpublished results by Dritschel, who found the value $|e/\omega_m|_c = 0.105$ based on contour dynamics simulations. Similar calculations (see e.g. Legras & Dritschel 1993) have shown that the critical value $|e/\omega_m|_c$ is independent of the vorticity distribution inside the vortex as long as the shape of the profile near the vortex centre is parabolic, which is generally the case for smooth vorticity distributions. For an exact parabolic profile $\omega^*(r^*) = 1-(r^*)^2$, with again r^* the vortex radius normalized by the appropriate position of peak velocity and $r^* \leqslant 1$, the mean vorticity as defined in (6.13) is equal to $2/3 \approx 0.667$ so that $|e/\omega_m|_c = 0.100$, which is close to the corresponding values mentioned above.

6.1.3. *Numerical algorithm*

A fourth-order Runge–Kutta method was applied to solve the equations of motion (6.1) and (6.2), in which the strain rate e was held constant and the uniform vorticity ω_0 was allowed to decay in time according to $\omega_0 = \bar{\omega} = 0.607\omega_m(t)$, with $\omega_m(t)$ representing expression (4.6). The free parameters in (4.6) and the strain rate e were obtained from experiment 6, and the state $(\lambda_0, \phi_0) = (1, 0)$ was taken as the initial

https://doi.org/10.1017/S0022112097006356 Published online by Cambridge University Press

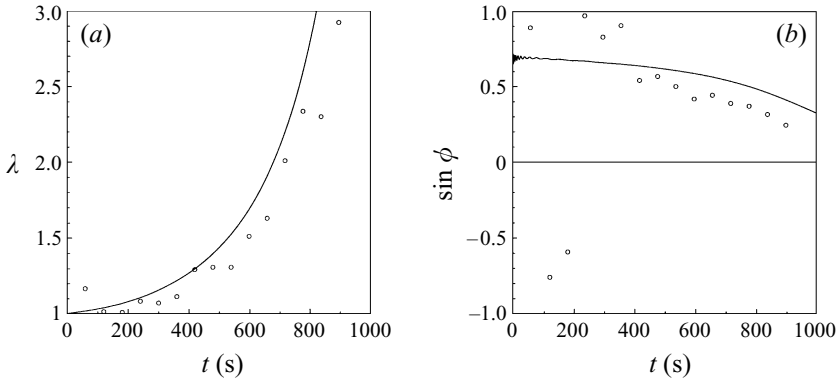


FIGURE 19. The aspect ratio λ and orientation ϕ versus time as obtained from the numerical integration (solid line) and the laboratory observations (circles). The integration was started at $t = \Delta t$ (Δt being the time step) with an initially circular patch of vorticity ($\boldsymbol{k}_0 = (1, 0)$) in a strain flow of strength $e = 0.303 \times 10^{-2}$ s^{-1}. The uniform vorticity ω_0 was allowed to decay according to $\omega_0 = 0.607\omega_m(t)$, where $\omega_m(t)$ corresponds to (4.6) with $C = 7.7$ cm^5 s^{-1}, $\nu = 1.065 \times 10^{-2}$ cm^2 s^{-1} and $t_0 = 227$ s. Experimental parameters: see table 2 (experiment 6).

condition. The numerical integration was performed with a time step $\Delta t = 0.05$ s. Because of the infinite vorticity at $t = 0$ (see (4.6)), the time integration was started at $t = \Delta t$, which only had a minor effect on the numerical results.

6.1.4. *Numerical results*

Figure 19 shows the numerical results (solid lines) for the time evolutions of λ and ϕ. Initially, the aspect ratio gradually increases, whereas the orientation of the vortex ϕ oscillates with high frequency. However, the amplitude and frequency of the fluctuations in ϕ are quickly damped, and in the next stage, $t > 300$ s, the angle ϕ gradually decreases with no more oscillations. Close to the critical value Λ_c at $t \approx 700$ s, the indefinite vortex tearing sets in, which is clear from the exponential increase of λ and the accelerated decrease of ϕ.

In order to make a comparison with the laboratory observations, the measured vorticity contours satisfying $\omega = \bar{\omega} = 0.607\omega_m$ were least-square fitted with ellipses, as described in § 5, for various moments of time. The measured aspect ratio λ ($= \lambda_\omega(\bar{\omega}, t)$) and orientation ϕ ($= \phi_\omega(\bar{\omega}, t)$) are plotted in figure 19 versus time, and are indicated by circles. The observed time evolutions of λ and ϕ deviate systematically from the corresponding calculated evolutions, but qualitatively the same behaviour is observed. For $t < 200$ s, large-amplitude oscillations are present for the observed orientation of the ellipse, which are less pronounced in the numerical simulation. These fluctuations are probably induced by the satellites of negative vorticity, which initially rotate around the vortex core before being detached by the ambient flow, an effect that is not dealt with by the vortex patch model. Part of the oscillation may also be caused by internal waves, which inevitably emerge during the forcing stage and the subsequent lifting of the sphere.

In § 5 it was argued that the indefinite vortex elongation is preceded by a quasi-stationary stage. Since Kida's model allows the stationary states to be calculated analytically, it is interesting to see how close the numerical solutions are to equilibrium before the indefinite elongation sets in. The vortex evolves along quasi-stationary states as long as the state $\boldsymbol{k}$ is close to the curve connecting the (local) extremal values of

https://doi.org/10.1017/S0022112097006356 Published online by Cambridge University Press

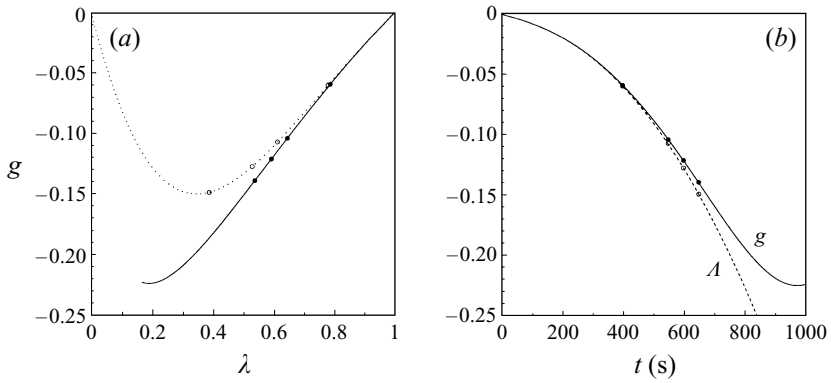


FIGURE 20. (*a*) Solution curve (solid line) in the (λ, g)-plane, corresponding to the evolution depicted in figure 19, and the stationary states (dotted line) as obtained analytically from the Kida model. (*b*) Comparison between the calculated evolutions of $g(t)$ (solid line) and $\Lambda(t)$ (dashed line). In both (*a*) and (*b*), the instantaneous states of the vortex patch (filled circles) are compared with the corresponding steady states (open circles) for four different times.

g, i.e. $\dot{\phi} \approx 0$, and its component g is close to one of the bounding values $\pm\Lambda$, so that $\dot{\lambda} \approx 0$.

Accordingly, in figure 20(*a*) the numerically obtained values of g (solid line) are plotted versus λ, as well as the curve corresponding with the (local) extremal values of g (dotted line). For convenience, the transformations $\lambda \to 1/\lambda$ and $g \to -g$ have been applied. It is seen that initially both curves coincide closely. When $\lambda \approx 0.8$ ($t \approx 400$ s) the numerical solution g starts to separate from the dotted line, but both curves are still close to each other up to $\lambda \approx 0.6$ ($t \approx 600$ s). After that, an accelerated deviation is observed around $\lambda = 0.5$ ($t = 700$ s). Thus, the calculated g-values are close to the dotted curve until the final stage of indefinite elongation. However, this assertion does not guarantee quasi-stationary solutions; it is a necessary but not sufficient condition for quasi-equilibrium states. The another requirement is that g is close to Λ. Therefore, the calculated time evolutions of g (solid line) and Λ (dashed line) are plotted in figure 20(*b*), and a good agreement is obtained between both curves until the vortex is torn apart at $t \approx 700$ s.

In order to make a direct comparison, in figure 20 the calculated states $\boldsymbol{k}$ and the corresponding equilibrium states have been marked by filled and open circles, respectively, at four different times. Again it is clear that the vortex evolves close to equilibrium states until the final breaking of the vortex by the strain flow.

6.2. *Modelling of a distributed vortex in a pure strain flow*

Experimental observations by Flór & van Heijst (1996) have revealed that monopolar vortices in a stratified fluid are characterized by a flat pancake-like shape. From a simple scaling analysis, it was shown that to leading order in Ri^{-1} vertical motions are decoupled from the horizontal motions, and vorticity vectors are approximately directed vertically in a thin region around the mid-plane ($z = 0$). Here, Ri represents the bulk Richardson number $Ri = N^2\sigma^2/U^2$, with 2σ the typical monopole thickness and U a characteristic horizontal velocity scale. Consequently, the three-dimensional vorticity equation around $z = 0$ could be reduced to

$$\frac{\partial \omega}{\partial t} + J(\omega, \psi) = \nu \nabla_h^2 \omega + \nu \frac{\partial^2 \omega}{\partial z^2}, \tag{6.15}$$

https://doi.org/10.1017/S0022112097006356 Published online by Cambridge University Press

with ω the vertical component of vorticity, ψ the stream function satisfying $\omega = -\nabla_h^2\psi$ (and appropriate boundary conditions), ∇_h the horizontal gradient operator, ν the kinematic viscosity, and the Jacobian J defined by

$$J(\omega,\psi) = \frac{\partial\omega}{\partial x}\frac{\partial\psi}{\partial y} - \frac{\partial\omega}{\partial y}\frac{\partial\psi}{\partial x}. \tag{6.16}$$

Because of this quasi-two-dimensional behaviour of the flow around the mid-plane $z = 0$, the vertical diffusion term in (6.15) will be modelled by an analytical expression, so as to solve (6.15) in only two dimensions. In finding such an analytical solution for the vertical diffusion term, it will be assumed that, to first approximation, the Jacobian in (6.15) is either close to zero or approximately linear, i.e. nonlinear effects are negligibly small. This assumption is supported by the observation that the laboratory vortex is initially close to circular ($J \approx 0$), and that subsequently, the vortex core evolves in a quasi-stationary manner ($J \approx 0$) for a considerable time. Although in the final stage of the evolution the Jacobian is definitely non-zero (which can be inferred from the scatter plots in figure 14), the vortex has then become so weak that advection is dominated by the background strain flow, i.e. the Jacobian is close to linear.

As in earlier studies (see Flór, van Heijst & Delfos 1995, Flór & van Heijst 1996 and Trieling & van Heijst 1997), the vorticity can now be written as

$$\omega(x,y,z,t) = \omega_{2D}(x,y,t)\Phi(z,t), \tag{6.17}$$

where $\omega_{2D}(x,y,t)$ represents the horizontal vorticity distribution satisfying the purely linear two-dimensional vorticity equation

$$\frac{\partial\omega_{2D}}{\partial t} + J(\omega_{2D},\psi) = \nu\nabla_h^2\omega_{2D}, \tag{6.18}$$

and $\Phi(z,t)$ is an amplitude function associated with the vertical diffusion of vorticity. Substitution of (6.17) in (6.15), neglecting nonlinear terms, reveals that the viscous decay of Φ is governed by

$$\frac{\partial\Phi}{\partial t} = \nu\frac{\partial^2\Phi}{\partial z^2}. \tag{6.19}$$

Initially, the vortex is assumed to be confined in a very thin region, represented by $\Phi(z,0) = \Phi_0\delta(z)$, with δ the Dirac delta function. The corresponding solution of the vertical diffusion equation (6.19) is then given by

$$\Phi(z,t) = \frac{\Phi_0}{(\nu t)^{1/2}}\exp\left(-\frac{z^2}{4\nu t}\right). \tag{6.20}$$

Although this delta-like initial condition cannot be satisfied in the actual flow, it is assumed that the thickness of the vortex at $t = 0$ is relatively small, and that at later times (6.20) still gives a reasonable description of the finite vertical vorticity distribution.

In the mid-plane, $z = 0$, the vertical diffusion term in (6.15) can now be expressed analytically, using (6.17) and (6.20), as

$$\nu\left.\frac{\partial^2\omega}{\partial z^2}\right|_{z=0} = \nu\,\omega_{2D}\left.\frac{\partial^2\Phi}{\partial z^2}\right|_{z=0} = -\left.\frac{\omega}{2t}\right|_{z=0}. \tag{6.21}$$

Hence, on substituting (6.21) in (6.15), the evolution of the (vertical) vorticity in the

https://doi.org/10.1017/S0022112097006356 Published online by Cambridge University Press

mid-plane $z = 0$ is approximately governed by

$$\frac{\partial \omega}{\partial t} + J(\omega, \psi) = \nu \nabla_h^2 \omega - \frac{\omega}{2t}, \tag{6.22}$$

$$\omega = -\nabla_h^2 \psi, \tag{6.23}$$

with suitable conditions for ψ on the boundaries of the domain in question. Expression (6.22) will henceforth be referred to as the quasi-two-dimensional vorticity equation. It should be emphasized that both (6.22) and (6.23) are evaluated at $z = 0$. Also note that nonlinear effects were neglected in deriving (6.21), but that these effects are still retained in the Jacobian of the quasi-two-dimensional vorticity equation.

Both (6.22) and (6.23) have been solved by a finite-difference method that is second-order accurate both in space and in time. The numerical scheme is based on that of Orlandi (1990), and has been slightly adapted to account for the vertical damping term and the ambient velocity field.

The time integration was performed by a third-order Runge–Kutta method, the Jacobian being calculated explicitly, while the horizontal and vertical diffusion terms were discretized by the implicit Crank–Nicolson scheme. The Jacobian J in (6.22) was evaluated by the so-called Arakawa scheme (see Arakawa 1966), which in the inviscid limit conserves the higher-order invariants of motion, such as energy and enstrophy. The implicit treatment of the horizontal diffusion term leads to a pentadiagonal matrix, the inversion of which is highly time consuming. Therefore, this matrix was decomposed into two tridiagonal matrices, which can be easily inverted by common solvers. Although this approach reduces the accuracy of the time integration to second order, the scheme has a larger stability regime than other commonly used second-order schemes, i.e. $CFL \leqslant \sqrt{3}$.

The solution of (6.23) was obtained by a FACR (Fourier Analysis and Cyclic Reduction) Poisson solver (see Hockney 1970) with the condition $\psi = exy$ at the boundary of the computational domain to account for the pure strain flow (note that the ambient flow contains zero vorticity).

The Cartesian coordinate system has been chosen such that the origin coincides with the stagnation point of the ambient flow, and that the x- and y-axes are oriented along the symmetry axes of the strain flow. The calculations were performed on a 256×256 grid, which proved to be accurate enough to resolve the vorticity field.

As an initial condition, the vorticity distribution (4.1) corresponding to the Gaussian vortex was chosen. Since the quasi-two-dimensional vorticity equation (6.22) is singular at $t = 0$, and the vorticity values are very large for small t (implying a very small time step to satisfy the CFL condition), the time integration was started at $t = 5$ s. The corresponding values for ω_m and r_m, which determine the instantaneous state of the Gaussian vortex, were obtained from the least-squares fits through the observed data as shown in figure 16. Strictly speaking, the vorticity distribution at $t = 5$ s is not represented by that of a Gaussian vortex. However, considering the small initial ratio e/ω_m, the contribution from the strain flow may be neglected at small times.

The typical flow evolution as obtained numerically is shown by the sequence of vorticity contour plots depicted in figure 21. Here, the initial conditions of experiment 6 have been used, and a similar behaviour is found to that observed in the laboratory (see figure 10). Initially, see figure 21 (*a*), the vortex is virtually unaffected by the ambient flow, given the nearly circular shape of the vortex. When time increases, see (*b*), the vortex becomes slightly distorted but is still close to circular. In the next stage (*c*–*g*), however, the emergence of two patches of negative vorticity and the removal

https://doi.org/10.1017/S0022112097006356 Published online by Cambridge University Press

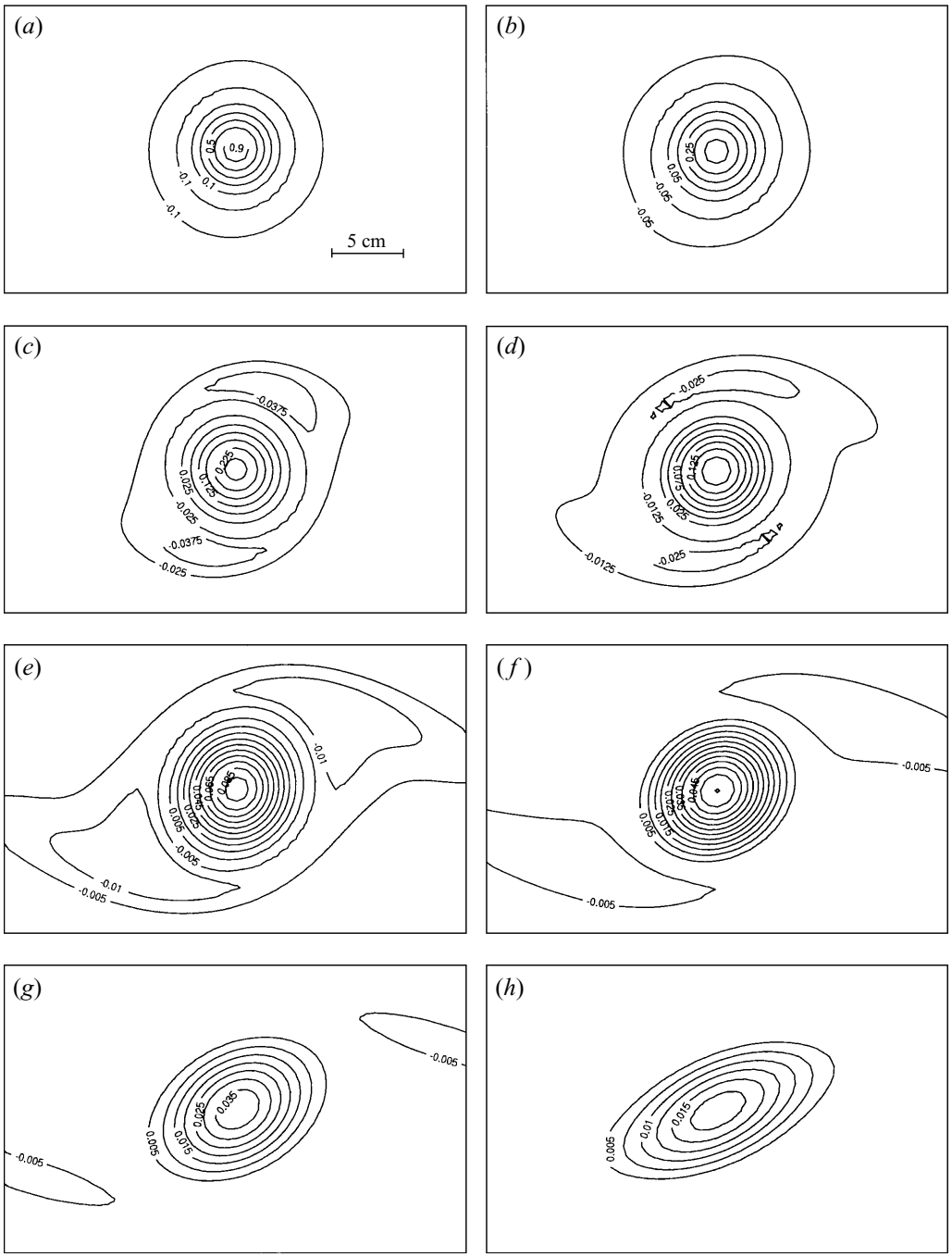


FIGURE 21. Sequence of vorticity contour plots as obtained from the numerical simulation of an isolated monopolar vortex in a pure strain flow (with $e = 0.30 \times 10^{-2}$ s^{-1}). The finite-difference calculations were performed on a 256×256 spatial grid within a 80 cm $\times$ 80 cm box. Furthermore, $\nu = 1.065 \times 10^{-2}$ cm^2 s^{-1} and $CFL = 0.5$. As an initial condition (at $t = 5$ s), a Gaussian vortex was taken with $\omega_m = 5.48$ s^{-1} and $r_m^2 = 4.93$ cm^2. (*a*) $t = 60$ s, (*b*) 120 s, (*c*) 180 s, (*d*) 240 s, (*e*) 360 s, (*f*) 480 s, (*g*) 600 s and (*h*) 840 s. The panels (*a*)–(*h*) have dimensions 32 cm $\times$ 20 cm, and may be compared with those depicted in figure 10.

https://doi.org/10.1017/S0022112097006356 Published online by Cambridge University Press

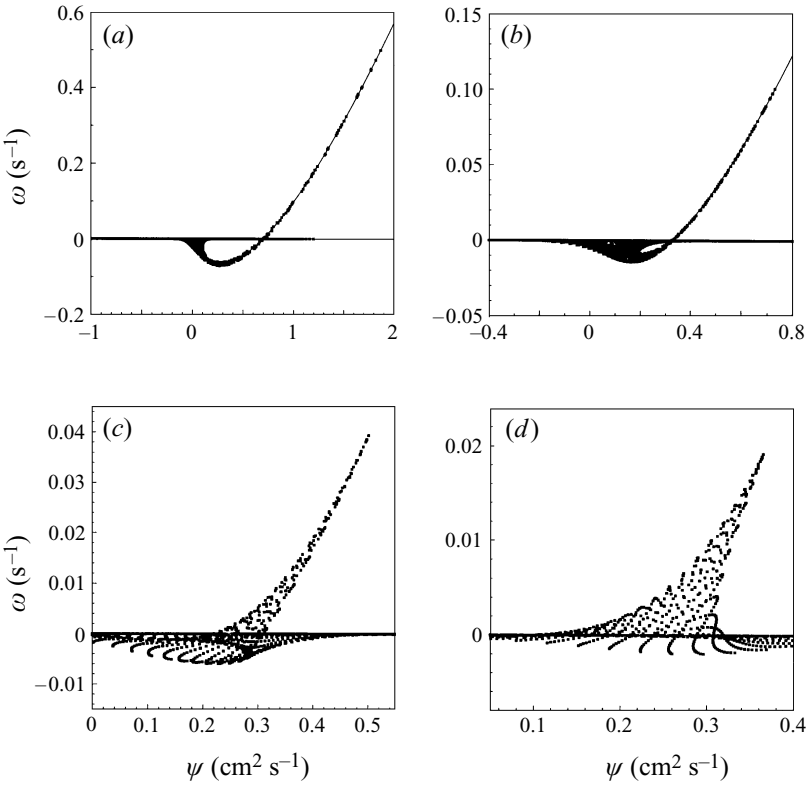


FIGURE 22. Sequence of numerically obtained (ω, ψ)-scatter plots: (*a*) $t = 120$ s, (*b*) 360 s, (*c*) 600 s and (*d*) 840 s. The same initial parameters were used as in figure 21. The solid line corresponds to the (ω, ψ)-relationship of the Gaussian vortex, and has been least-square fitted to the numerical data for $\omega > 0.25\omega_m$. The maximum vorticity decreased from $\omega_m = 0.50$ s^{-1} at $t = 120$ s to $\omega_m = 0.019$ s^{-1} at $t = 840$ s. The results may be compared with those in figure 14.

of negative vorticity by the strain flow are obvious. Finally, see (*h*), the vortex is rotated towards the horizontal strain axis and is eventually torn apart. Comparison with figure 10 reveals that the advection of negative vorticity occurs faster in the laboratory than in the numerical simulation. Also the final rotation speed of the vortex is larger experimentally than numerically. The differences may be explained by the non-uniformity of the experimental strain flow, which will be discussed later on.

Laboratory observations presented in § 5 have demonstrated that the vortex core evolves quasi-steadily until the final stage of indefinite elongation. A sequence of numerically obtained (ω, ψ)-scatter plots is shown in figure 22, and a good agreement is observed with the experimental results presented in figure 14. The scatter in figure 14 is more pronounced because of the experimental errors and the faster evolution of the laboratory vortex. From figure 22, it is also evident that initially the positive branch of the calculated scatter plots is in good agreement with the (ω, ψ)-relationship associated with the Gaussian vortex (solid lines in figure 22 *a, b*).

In figure 16, the numerically obtained decay of the maximum vorticity (dashed lines) is compared with the experimental data (indicated by symbols), and a good agreement is observed for each experiment. In addition, the numerical results closely match the least-squares fits (solid lines) related to (4.6) until the vortex is overcome by the strain flow. This is most clear from the data corresponding to experiment 7

https://doi.org/10.1017/S0022112097006356 Published online by Cambridge University Press

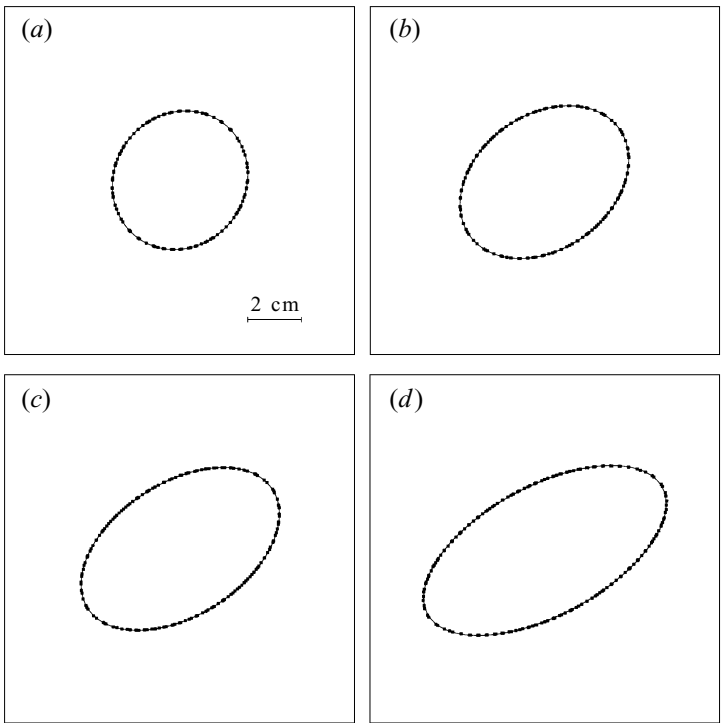


FIGURE 23. Typical discretized vorticity contours $\omega = \bar{\omega} = 0.607\omega_m$ of a vortex in a strain flow at four different times: (*a*) $t = 420$ s, (*b*) 600 s, (*c*) 720 s and (*d*) 840 s. A perfect elliptic contour (solid line) has been been fitted to each numerically obtained contour. Numerical parameters as in figure 21.

(triangles). Around $t = 400$ s ($|e/\omega_m| \approx |e/\omega_m|_c$), the calculated curve departs from the least-squares fit, but still closely follows the experimental data. These results support the assertion that the initial decay of the maximum vorticity is not affected by the strain flow and is accurately described by (4.6).

In order to make a quantitative comparison between the experiments and the numerical simulations, the numerically obtained vorticity contours $\omega = \bar{\omega} = 0.607\omega_m$ were discretized and least-square fitted with ellipses, using the same method as described in § 5. Figure 23 shows typical discretized vorticity contours corresponding to the intermediate and the final stages of the vortex evolution, and the contours clearly resemble perfect ellipses. These ellipses were used to determine the major and minor axes (a and b), the aspect ratio (λ) and the inclination (ϕ) for a sequence of times.

The calculated evolutions of the major and the minor axes (a and b) are indicated in figure 24(*a*) by the solid and dashed lines, respectively. Initially, both a and b increase monotonically and are very close to each other. However, at a later stage, an accelerated growth of a is observed, whereas b eventually decreases in time. In order to understand this behaviour, the product ab, which represents the area of the specific ellipse, is plotted in figure 24(*b*) (solid line) along with the evolution of the growing area r^2 of a vortex in still ambient fluid (dotted line). To be more specific, r^2 represents the area enclosed by the circular vorticity contour $\omega = \bar{\omega}$, the radial expansion of which is exclusively caused by horizontal diffusion (note that $r^2 \sim r_m^2 = r_0^2 + 2\nu t$, which can be derived from (4.1) and (4.5)).

https://doi.org/10.1017/S0022112097006356 Published online by Cambridge University Press

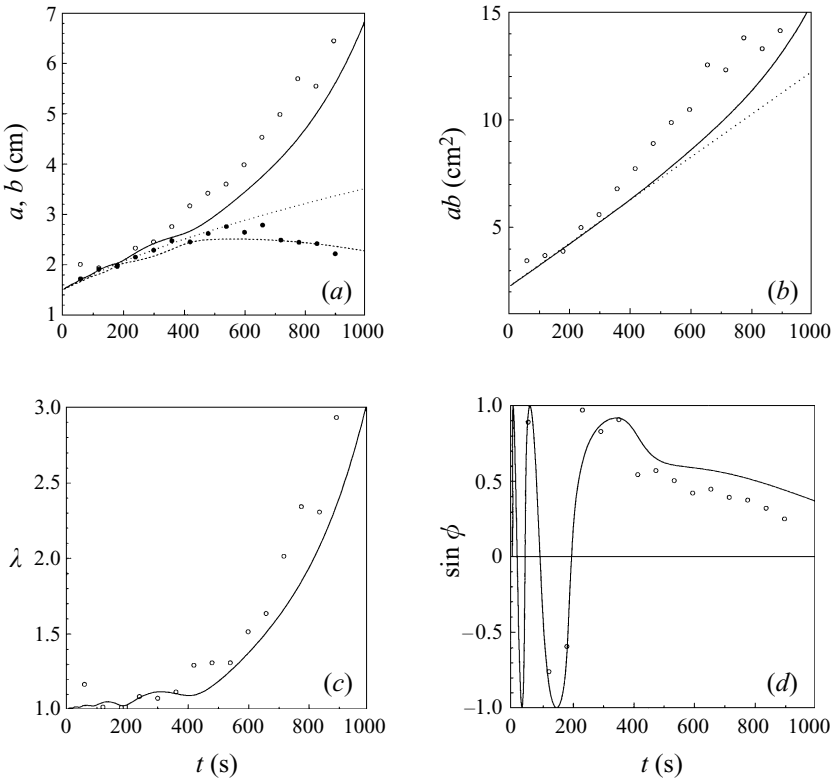


FIGURE 24. (*a*) Graph showing the calculated time evolution of the principal axes a and b, which are represented by the solid and dashed lines, respectively. The experimentally obtained evolutions of a and b are indicated by the open and filled circles, respectively. Also shown are the temporal evolution of the area ab (*b*), the aspect ratio λ (*c*), and the orientation ϕ (*d*); the calculated values are indicated by solid lines, whereas the observed data are represented by open circles. The dotted lines represent the radial expansion of a Gaussian vortex without background flow. All values have been obtained from the discretized vorticity contour $\omega = 0.607\omega_m$, and the same numerical parameters have been used as in figure 21.

Initially, the values of ab coincide with the curve $r^2(t)$, which means that the growth of the elliptic area is caused purely by horizontal diffusion. However, at a later stage ($t \approx 400$ s), ab increases faster than predicted by pure horizontal diffusion. This additional growth of ab may be due to an accelerated outward diffusive flux of vorticity. In figure 21 it was shown that the ring of negative vorticity is carried away by the strain flow. Since the presence of this ring opposes the radial expansion of the vortex, the accelerated diffusive flux is probably caused by the removal of surrounding negative vorticity. Similar results were obtained by Mariotti *et al.* (1994) in their numerical study on monopolar vortices (of single-signed vorticity) in a shearing background flow.

In figure 24 (*a*), the time evolutions of a and b are compared with the radial growth $r(t)$ of a vortex in still ambient fluid (dotted line). At first, both a and b are close to $r(t)$ and show weak-amplitude oscillations, but later on, the values of the principal axes diverge from the curve corresponding to pure viscous diffusion. By plotting the aspect ratio $\lambda = a/b$ against time in figure 24 (*c*), it is obvious that this divergence is due to the elongation of the vortex. Likewise, the weak amplitude oscillations in a and b are related to the shape oscillations of the vortex. Hence, figure 24 (*a*) shows

https://doi.org/10.1017/S0022112097006356 Published online by Cambridge University Press

the strain-induced evolution of the principal axes superimposed on the pure diffusive expansion of the vortex.

In figure 24 (*d*), the calculated orientation of the vortex is plotted versus time (solid line). Initially, the vortex rotates around its centre until $t \approx 350$ s, at which time the rotation speed has decreased to zero ($\dot{\phi} = 0$). The rotational motion can be explained by the presence of the two satellites of negative vorticity which surround the vortex core. This situation is very similar to that of a tripolar vortex, as observed in the laboratory by Kloosterziel & van Heijst (1991), which rotates around its centre in a solid-body-like fashion. In the next stage, the vortex rotates backwards, though its orientation remains close to 45° with respect to the horizontal strain axis. During this stage, the satellites are being separated from the vortex by the ambient flow. Finally, after $t \approx 700$ s, the rotation accelerates and the vortex turns towards the horizontal strain axis.

Figure 24 (*a*) also shows the evolution of the axes a and b as observed in the laboratory (indicated by open and filled circles, respectively). Initially, the measured data are in good agreement with the numerical results, but for larger times ($t > 300$ s), the observed data overshoot the numerically obtained values. In figure 24 (*b*) a similar behaviour can be observed: after $t \approx 300$ s, the measured elliptic area ab increases faster than expected from the numerical model.

The measured values of λ and ϕ are plotted versus time in figures 24 (*c*) and 24 (*d*), respectively. Taking into account the experimental errors, which are estimated to be about 10–20% for small values of λ, in each case a good agreement is obtained with the calculated evolution for a long time. In the final stage of the evolution, however, the vortex elongation and vortex tumbling proceed faster than expected from the numerical model.

A few possible causes may be considered for the accelerated evolution of the laboratory vortex. First, the growing strain rate e was neglected in the numerical model, whereas the strain rate measurements (see figure 7) indicate that e increases about 5–10% during the whole vortex evolution (assuming that the growth of the strain rate is not affected by the presence of the vortex). However, a second numerical simulation, in which the strain rate was allowed to increase by 10% between $t = 0$ and $t = 1000$ s, demonstrated that this effect gives only a minor contribution to the vortex evolution, and cannot explain the deviations with the experiments completely.

Secondly, the dynamics in the computational domain may be different from that in an infinite plane: the numerical boundary conditions impose a pure strain flow along the boundaries, which is actually wrong if non-zero vorticity is present within the bounded domain. Therefore, another numerical simulation was performed in which the size of the computational domain was doubled and a 512×512 grid was used to retain the resolution. However, no significant difference could be observed with the former simulations.

It may also be that the three-dimensional evolution of the laboratory vortex is only partly represented by the source solution (6.20). Since detailed measurements of the vertical motion are lacking, it is difficult to draw conclusions about the influence of additional three-dimensional effects. Nevertheless, the calculated decay of the maximum vorticity is in good agreement with the experimental data, as can be inferred from figure 16. Moreover, laboratory observations by Trieling & van Heijst (1997) have shown that the evolution of a monopolar vortex in still ambient fluid is accurately described by the present model.

The faster destruction of the laboratory vortex may be ascribed to the non-

https://doi.org/10.1017/S0022112097006356 Published online by Cambridge University Press

uniformity of the experimental strain flow. As can be inferred from figures 6(*c*) and 6(*d*), the local strain rates near the discs are larger than the uniform strain rate near the centre of the flow field. Consequently, the velocities near the discs are also larger than expected from the central part of the flow domain. This effect is illustrated most clearly by the accelerated advection of negative vorticity, as observed in the laboratory. Because of the horizontal expansion and the fast growing aspect ratio of the vortex, part of the vortex core may fall into the intensified strain rate region, which will result in both an accelerated elongation and a faster rotation of the vortex.

7. Conclusions

In this paper, the dynamics of monopolar vortices in a strain flow was investigated based on laboratory experiments that were performed in a stratified fluid. The laboratory observations revealed that the evolution of shielded monopolar vortices in a strain flow is characterized by the initial deformation of the vortex into a tripolar-like structure, followed by the shedding of the accompanying satellites. In the next stage, the vortex was observed to evolve quasi-steadily, as evident from the (ω, ψ)-scatter plots. Finally, the vortex was torn apart along the horizontal strain axis owing to the diffusive decay of vorticity. This behaviour appeared to be independent of the absolute strain rate, which only determined the speed of the vortex evolution, but not the evolution process itself.

The dynamics of the vortex core was very similar to that of an elliptic patch of uniform vorticity in a strain flow. At high vorticity amplitudes the instantaneous vorticity contours were close to ellipses with nearly the same aspect ratios and orientations. Moreover, the laboratory observations were generally in good qualitative agreement with the calculated vortex evolution according to the extended Kida model.

The preservation of the elliptic shape of the vortex core is consistent with the fact that elliptic shapes are preserved in a pure strain flow (see Kida 1981 and Legras & Dritschel 1991). This assertion is supported by numerical simulations of non-uniform vortices in strain and shear flows (see Legras & Dritschel 1993, 1994), in which the shapes of the higher-vorticity contours were observed to remain close to elliptic. It is worth mentioning that nearly elliptic vortices were also found in numerical simulations by Melander *et al.* (1987), who considered the relaxation of smooth elliptic vorticity distributions towards axisymmetry, and in laboratory experiments by Hernan & Jimenez (1982), who observed elliptic-like vortex structures in free-shear layers.

As a second approach, the quasi-two-dimensional vorticity equation was solved numerically by a finite-difference method to account for both the non-uniform vorticity distribution of the laboratory vortex and the horizontal diffusion of vorticity. The calculated vortex evolution was very similar to that observed in the laboratory. Furthermore, it was shown that the removal of the surrounding negative vorticity induces an accelerated horizontal growth of the vortex, which was also observed in a numerical study by Mariotti *et al.* (1994). Owing to the non-uniformity of the experimental strain flow, the laboratory vortex evolved faster than in the numerical simulation.

We are grateful to Dr Roberto Verzicco for providing the finite-difference code, and for helpful suggestions on some numerical problems. One of the authors (R.R.T.) gratefully acknowledges financial support by the Foundation for Fundamental Research on Matter (FOM) of the Netherlands Organization for Scientific Research (NWO).

https://doi.org/10.1017/S0022112097006356 Published online by Cambridge University Press

REFERENCES

Arakawa, A. 1966 Computational design for long term numerical integration of the equations of fluid motion: Two-dimensional incompressible flow. Part I. *J. Comput. Phys.* **1**, 119–143.

Brickman, D. & Ruddick, B. R. 1990 The behavior and stability of a lens in a strain field. *J. Geophys. Res.* **95**, 9657–9670.

Chaplygin, S. A. 1899 On a pulsating cylindrical vortex. *Trans. Phys. Sect. Imperial Moscow Soc. Friends of Natural Sciences* **10**, N 1, 13–22. Also In *Collected Works*, 1948, vol. 2, pp. 138–154 (in Russian). German abstract: Über einen pulsierenden cylindrischen Wirbel, *Jahrbuch über die Fortschritte der Mathematik* (Jahrgang 1899), 1901, **30**, 683–684.

Dalziel, S. 1992 *DigImage. Image Processing for Fluid Dynamics.* Cambridge Environmental Research Consultants Ltd.

Dritschel, D. G. 1989 Strain-induced vortex stripping. In *Mathematical Aspects of Vortex Dynamics* (ed. R. E. Caflisch), pp. 107–119. Society of Industrial and Applied Mathematics.

Dritschel, D. G. 1995 A general theory for two-dimensional vortex interactions. *J. Fluid Mech.* **293**, 269–303.

Flór, J. B. & Heijst, G. J. F. van 1996 Stable and unstable monopolar vortices in a stratified fluid. *J. Fluid Mech.* **311**, 257–287.

Flór, J. B., Heijst, G. J. F. van & Delfos, R. 1995 Decay of dipolar structures in a stratified fluid. *Phys. Fluids* **7**, 374–383.

Hernan, M. A. & Jimenez, J. 1982 Computer analysis of a high speed film of the plane turbulent mixing layer. *J. Fluid Mech.* **119**, 323–345.

Hockney, R. W. 1970 The potential calculation and some applications. In *Methods in Computational Physics* (ed. B. Alder, S. Fernbach & M. Rotenberg), vol. 9, pp. 135–211. Academic Press.

Kida, S. 1981 Motion of an elliptic vortex in a uniform shear flow. *J. Phys. Soc. Japan* **50**, 3517–3520.

Kirchhoff, G. 1876 *Vorlesungen über mathematische Physik: Mechanik.* Teubner.

Kloosterziel, R. C. & Heijst, G. J. F. van 1991 An experimental study of unstable barotropic vortices in a rotating fluid. *J. Fluid Mech.* **223**, 1–24.

Legras, B. & Dritschel, D. G. 1991 The elliptical model of two-dimensional vortex dynamics. I: The basic state. *Phys. Fluids* A **3**, 845–854.

Legras, B. & Dritschel, D. G. 1993 Vortex stripping and the generation of high vorticity gradients in two-dimensional flows. *Appl. Sci. Res.* **51**, 445–455.

Legras, B. & Dritschel, D. G. 1994 Vortex stripping. In *Modelling of Oceanic Vortices* (ed. G. J. F. van Heijst), pp. 51–59. North Holland.

Mariotti, A., Legras, B. & Dritschel, D. G. 1994 Vortex stripping and the erosion of coherent structures in two-dimensional flows. *Phys. Fluids* **6**, 3954–3962.

Melander, M. V., McWilliams, J. C. & Zabusky, N. J. 1987 Axisymmetrization and vorticity-gradient intensification of an isolated two-dimensional vortex through filamentation. *J. Fluid Mech.* **178**, 137–159.

Meleshko, V. V. & Heijst, G. J. F. van 1994 On Chaplygin's investigations of two-dimensional vortex structures in an inviscid fluid. *J. Fluid Mech.* **272**, 157–182.

Moore, D. W. & Saffman, P. G. 1971 Structure of a line vortex in an imposed strain. In *Aircraft Wake Turbulence and its Detection* (ed. J. H. Olsen, A. Goldburg & M. Rogers), pp. 339–354. Plenum.

Nguyen Duc, T. & Sommeria, J. 1988 Experimental characterization of steady two-dimensional vortex couples. *J. Fluid Mech.* **192**, 175–192.

Orlandi, P. 1990 Vortex dipole rebound from a wall. *Phys. Fluids* A **2**, 1429–1436.

Overman, E. A. & Zabusky, N. J. 1984 Diagnostic algorithms for contour dynamics. In *Trans. First Army Conf. on Appl. Maths and Computing. ARO Rep.* 84-1, pp. 269–287.

Paihua Montes, L. 1978 Methodes numériques pour le calcul de fonctions-spline à une ou plusieurs variables. Thèse de 3^{e} cycle, Université de Grenoble, France.

Paireau, O., Tabeling, P. & Legras, B. 1997 A vortex subjected to a shear: an experimental study. *J. Fluid Mech.* (in press).

Polvani, L. M., Wisdom, J., DeJong, E. & Ingersoll, A. P. 1990 Simple dynamical models of Neptune's Great Dark Spot. *Science* **249**, 1393–1398.

Trieling, R. R. & Heijst, G. J. F. van 1997 Decay of monopolar vortices in a stratified fluid. *Fluid Dyn. Res.* (in press).

https://doi.org/10.1017/S0022112097006356 Published online by Cambridge University Press